<u>Diplomarbeit</u>

Geometrical influences on magnetic fields

Ausgeführt am Institut für Festkörperphysik der Technischen Universität Wien

unter der Anleitung von Priv. Doz. Dieter Suess und Dr. Florian Bruckner

durch

Raphael Thanhoffer

Pfeilgasse 16/1/7, 1080 Wien

Wien, 14. 5. 2014   Raphael Thanhoffer

OVERVIEW

Working with magnetic materials is a quite sophisticated case: Not only one has to take care of all the values from the datasheets, but also geometrical circumstances need to be taken into account. The possibility to combine hard and soft magnetic materials in to one device makes matters even more delicate. This leads to a high demand in powerful numerical simulation tools, like FEMME – which is also the most important tool used in this thesis.

Soft magnetic cones

Varied cone height
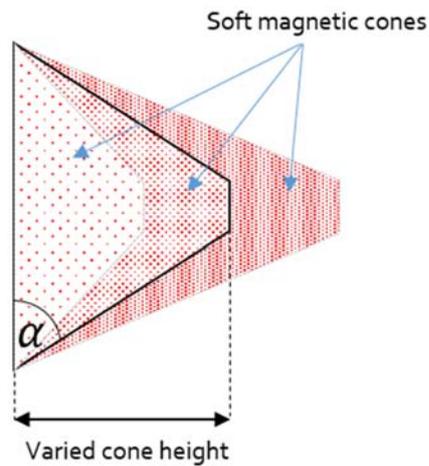
Soft magnetic materials are often used to amplify magnetic fields to make them detectable for sensors. In this case, the geometry of the soft magnetic material is of high importance. In this thesis the shape of a standard flux concentrator was optimized with respect to field strength. In particular, an optimal tip angle for such a sensor was found. This knowledge was later used to build a device that can increase the magnetic field of a high quality $Nd_2Fe_{14}B$ magnet by a factor larger than two.

To verify some computational FEMME simulations, an experimental setup was built. Within it, the magnetic fields using three different cone angles are measured. The simulation predicts that values of $3.5\ T$ can be achieved. The main goal of this setup is to prove that using geometrical advantages can boost magnetic field strength beyond the saturation point of the soft magnetic material. In this case, a value above $3.0\ T$ (which is $50\ \%$ above the J_s of iron) would be a success.

ABSTRACT

When using iron to concentrate the flux, we deal with two areas of significant interest: The linear one, where the soft magnetic material (usually iron) is used as an easy predictable amplifier, which increases very small fields by some magnitudes in order to make them measurable. On the other hand, the saturated case, in which one can produce field strengths much higher than the saturation magnetization with the help of geometrical optimization. Both cases were investigated with the help of numerical simulations using the finite element method based software FEMME. Therefore the open source software Salome was used to draw geometries and alter those, using python scripts which were able to change some parameters of given geometries (like an angle) and restart the simulation.

The very strong influence of the shape of an object and its resulting magnetic field strength was shown for different cases of hard magnetic, but also hard and soft magnetic material combinations – nowadays an often used approach. When using flux field concentrators made from materials with very high saturation magnetizations like iron ($J_s > 2.0\ T$), a suboptimal shape of the flux field concentrators can influence the resulting field strength significantly. It was shown, that comparable small fields of $0.1\ T$ are sufficient to almost saturate shape optimized iron flux concentrators, which results in very high amplification factors of the measured field. This is of high importance, when measuring very weak magnetic fields with sensors.

The results of the maximum field strength simulations were also verified by an experimental setup, which was used to validate the simulations. Fields of almost $3.5\ T$ were measured, which is more than twice the saturation magnetization of a high quality $Nd_2Fe_{14}B$ magnet ($J_s = 1.43\ T$).

KURZFASSUNG

Bei der Verwendung von Eisen als Flussfeldkonzentrator sind zwei Bereiche besonders voneinander zu unterscheiden: Der lineare Bereich, in dem das weichmagnetische Material (zumeist Eisen) als gut berechenbarer Verstärker dient und sehr kleine Felder zu Messzwecken um einige Größenordnungen verstärken kann, sowie der gesättigte Bereich, in dem man Felder weit über der Sättigungsmagnetisierung mithilfe von geometrischen Optimierungen realisieren kann. Beide Fälle wurden mithilfe numerischer Simulationen unter der Verwendung der auf der finiten Elemente Methode aufbauenden Software FEMME untersucht. Dafür wurden Python Scripts für die open Source Software Salome entwickelt. Diese erlauben einen Körper zu parametrisieren und die automatische Erstellung eines Finite-Elemente-Gitters.

Deutlich sichtbar wurde der starke Einfluss der Geometrie auf die resultierende magnetische Feldstärke, für den Fall von verschieden geformten hartmagnetischen, aber auch bei der Kombination von hart- und weichmagnetischen Materialien – was heutzutage eine gängige Vorgehensweise darstellt. Beim Einsatz von Flussfeldkonzentratoren aus weichmagnetischem Material wie beispielsweise Eisen ($J_s > 2.0\,T$) kann eine suboptimale Form der Flussfeldkonzentratoren die Stärke des resultierenden Magnetfeldes massiv beeinträchtigen und eventuelle Leistungssteigerungen die man sich mit der Wahl von teuren Materialien erkauft komplett zunichtemachen.

Es wurde nachgewiesen, dass auch vergleichsweise schwache Felder von $0.1\,T$ genügen, um formoptimierte Flussfeldkonzentratoren aus Eisen zu sättigen und damit sehr hohe Verstärkungsfaktoren zu generieren. Als Anwendung ist das in erster Linie für die Messung schwacher magnetischer Felder von hoher Wichtigkeit.

Im Falle der maximalen Flussdichte wurde außerdem eine experimentelle Verifikation durchgeführt, deren Ergebnisse die berechneten verifizierten. Dabei wurden Felder von annähernd $3.5\,T$ gemessen, was mehr als der doppelten Sättigungsmagnetisierung eines guten $Nd_2Fe_{14}B$ Magneten ($J_s = 1.43\,T$) entspricht.

CONTENTS

1. ABBREVIATIONS AND DEFINITIONS

The abbreviations used in this thesis are constantly reused. Here one can find a quick overview of the often used ones:

$\vec{M}$	...	magnetization
$\vec{H}$	...	magnetic field strength
$\vec{B}$	...	magnetic induction
μ_0	...	magnetic constant (vacuum permeability)
μ^+/μ^-	...	permeability in/outside a material
$\mu_r = \frac{\mu}{\mu_0}$	...	relative permeability
χ	...	susceptibility
J_s	...	saturation / polarization
$\vec{H}_{Ext}$	...	external applied magnetic field
$\nabla u^+ / \nabla u^-$	...	stray field in/outside a material
N	...	demagnetization factor
G	...	gain factor
$\vec{A}$	...	vector potential
$\vec{I}$	...	electric current
$A_H = \frac{1}{nq}$	...	Hall constant
$\vec{J}$	...	current density
q	...	charge
U	...	voltage
Φ	...	potential
$\vec{H}_D$	...	demagnetizing field
M_S	...	saturation magnetization

In general the thesis relies on the SI definitions of physical constants (1).

2. INTRODUCTION

Magnetic materials can be characterized and compared with respect to certain unit properties given by a hysteresis loop. The hysteresis for a certain material describes the dependence of its magnetization $\vec{B}$ in relation to a external field $\vec{H}$ (2). From every hysteresis loop for a magnetic material we can read: B_R (remanence), B_S (saturation) and H_C (corecivity) which are intrinsic parameters of a material (3).
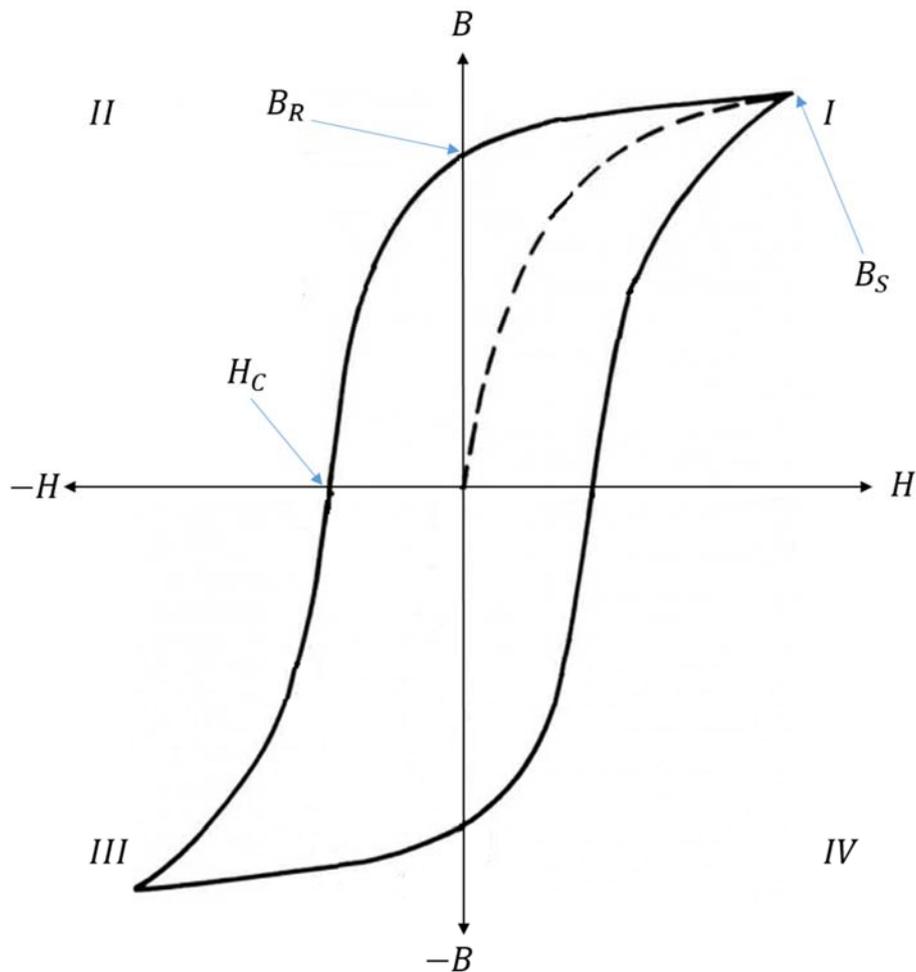
GRAPH 1: HYSTERESIS LOOP AND IMPORTANT VALUES

There are two main options when working with a magnet: In its saturated regime, it can be used for creating maximum magnetic fields - for adiabatic magnetization processes (4), or recording heads for hard drives (5) for example. Alternatively one can use the magnet in its linear regime (compare Graph 5: Linear and saturated areas of a material) to amplify a magnetic field for measuring purposes (6). This kind of sensors are used in a wide range from automotive applications (7), nanotechnology (8) and many more to come (9), (10).

Many of the applications above have one thing in common: The higher the magnetization of the material, the better the achieved results will be. Therefore this thesis shall give some simple advices when dealing with this kind of problems, regarding the geometrical shapes of the materials one works with. The results are based on simulations and experiments, tough most of the work has been done with FEMME ((11), or see chapter "FEMME").

2.1 LOAD LINE AND OPERATING POINT

When using a magnetic material as permanent magnet, the probably most important value is the load line or operating point. It indicates, how much of the magnets field can be measured on the outside and therefore be used for an experiment or an application.

The operating point can be obtained from the second quadrant of the hysteresis (if you look at Graph 1: Hysteresis loop and important values it would be the quadrant $-H/B$). Here it is important to note, that the hysteresis loop was measured in a closed loop, such as a ring. This is important, because in a closed ring (or even better a donut formed sample) no internal stray fields act on the magnetization (demagnetization factor $N = 0$). With:

$$\vec{H}_D = -N\vec{M} \tag{2.1}$$

And:

$$\vec{H} = \vec{H}_{Ext} - N\vec{M}$$

Where N is the demagnetizing factor (see chapter "Flux concentration") and $\vec{M}$ the magnetization. To get to the operating point, we simply find our values for N (12), (13) and multiply them with $\vec{M}$, which is usually easy to find in every datasheet of a permanent magnet. At $\vec{B}(\vec{H}_D)$ we find the working point as shown in Graph 2: Operating point and load line.

The load line is constructed as straight line intersecting the coordinate origin ($H = 0/B = 0$) and the working point. Mathematically this would read as:

$$\vec{B} = \mu_0(\vec{H}_D + \vec{M}) \tag{2.2}$$

The values are now of scalar nature, as the hysteresis loop is always measured in one particular direction (with $M = -\frac{1}{N}H_D$)

$$-\frac{B}{H_D} = \mu_0 \frac{1-N}{N} \tag{2.3}$$
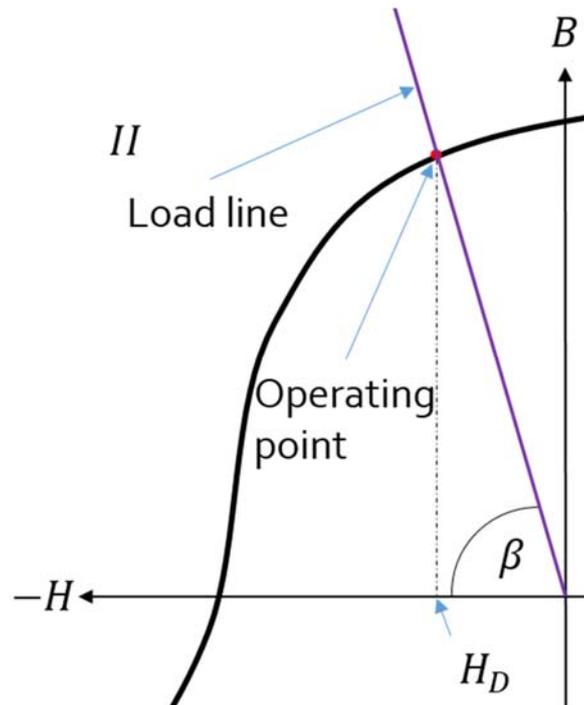
GRAPH 2: OPERATING POINT AND LOAD LINE

The load line itself is important for dynamic systems, where the angle β changes.

2.2 HARD AND SOFT MAGNETIC MATERIALS

Ferromagnetic materials can be divided into so called hard and soft magnetic materials. The name comes from the fact that the hard magnetic materials are harder to demagnetize than the soft magnetic materials. A closer look to the hysteresis rapidly explains why.
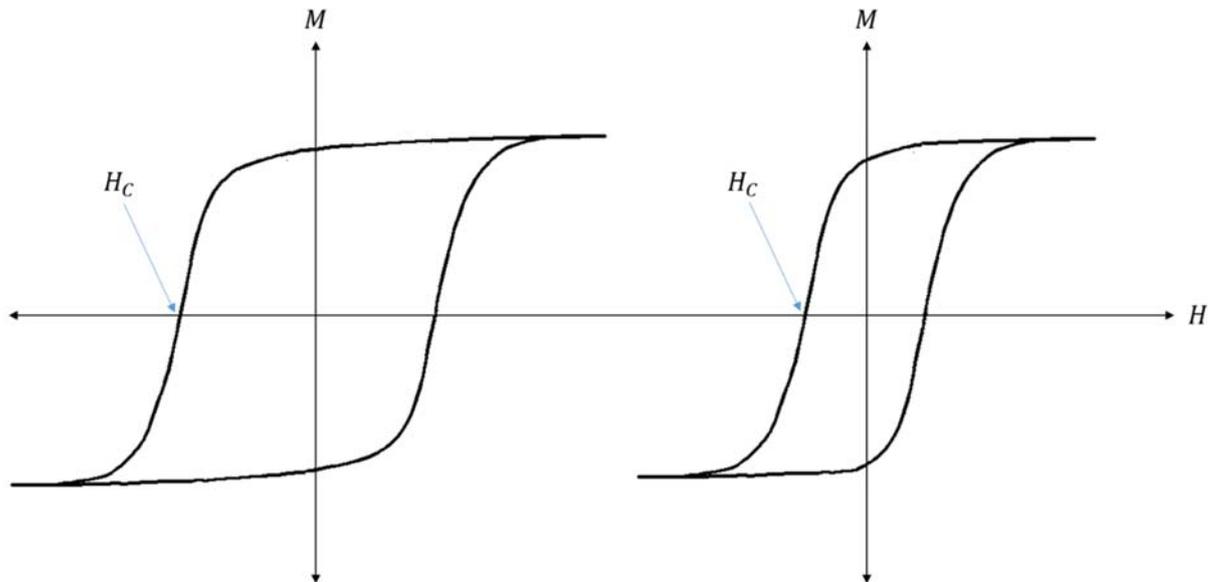
GRAPH 3: HARD AND SOFT MAGNETIC MATERIAL IN COMPARISON

The bigger value of H_C for the hard magnetic material means, it will stay magnetized permanently. These materials are subjected to special processing in powerful magnetic fields during manufacture, to align the microcrystalline structures. On the other hand, soft magnetic materials tend to be magnetized easily, but the magnetization is lost, as soon as the external field is turned off.

When putting a magnetized hard magnetic material in a magnet field $H_{Field} > H_C$ the materials magnetization can be revered in direction. Because the H_C is much smaller for a soft magnetic material, it takes a smaller external field to reverse the direction of the magnetization.

After an external field is applied and shut off, the magnetic material is always left with its remanence B_R (as seen in Graph 1: Hysteresis loop and important values). This effect is usually used to provide the magnetic memory in magnetic storage devices (14), and is used as a source of information on the past earth's magnetic field in paleomagnetism (15).

2.3   DESHEARING

FEMME uses hysteresis data as material properties, which look different than a typical hysteresis of a material, you can find in a data sheet (compare chapter "Iron-cones") for example. The reason is the so called effect of deshearing. It comes from the fact, that in data sheets the hysteresis is plotted with $\vec{H}_{Ext}$ over $\vec{B},\vec{M}$ or $\vec{J}$, where in the calculations (in FEMME for example) the $\vec{H}$ is often defined as $\vec{H} = \vec{H}_{Ext} - \nabla u$.
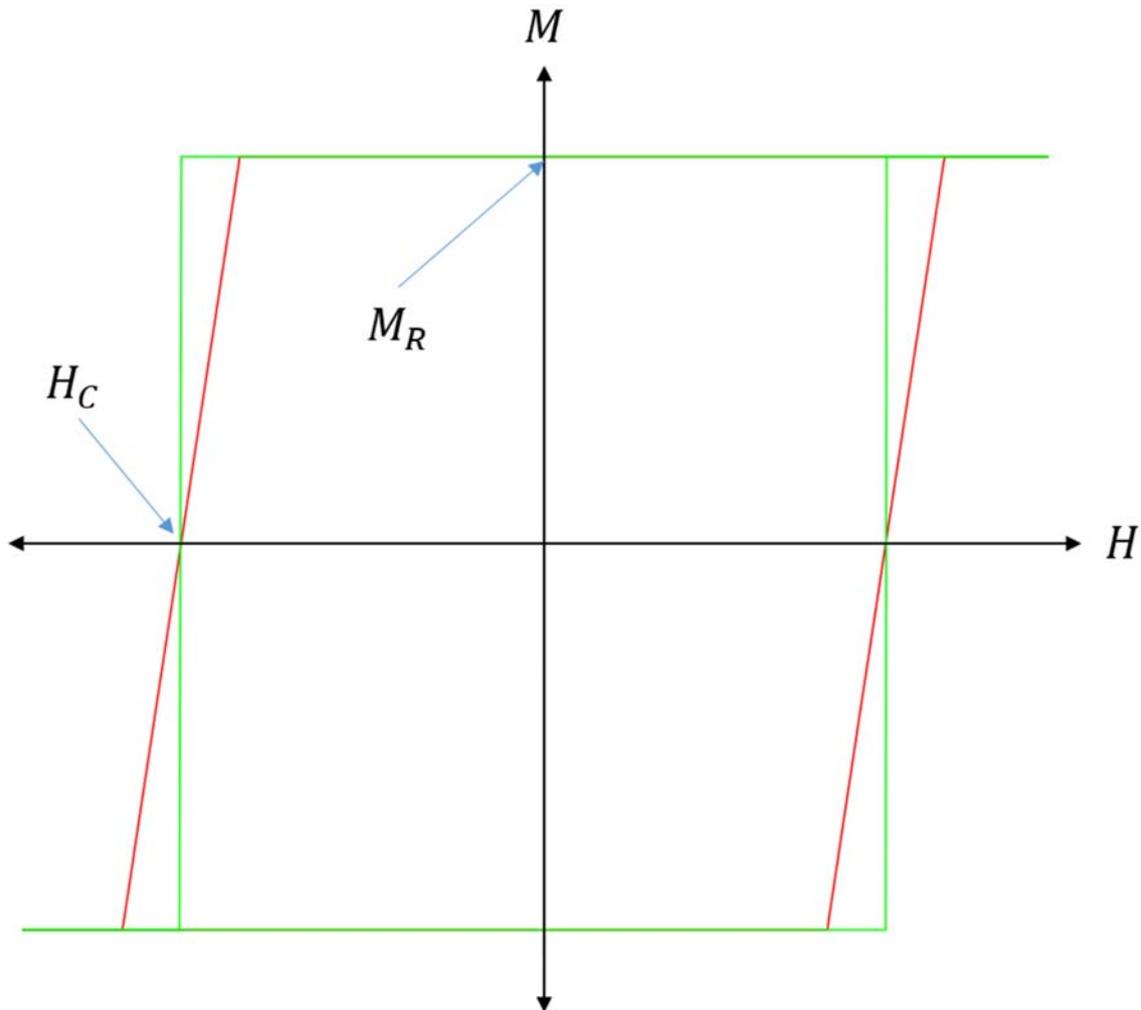
In Graph 4: Sheared (geometry dependent, red) and unsheared (geometry undependent, green) hysteresis two hysteresis loops of the same material are shown. Also the corecitivity H_C and the remanence M_R are shown. The red line indicates a hysteresis that could be obtained by measuring a sample, the green line comes from a calculated line, which is used by FEMME (or a measurement in a closed loop) for example. The different form of the lines can be explained by looking at the different forms of $\vec{H}$ in this graph:

$$\vec{H} = \vec{H}_{Ext} - N\vec{M} \qquad (2.4)$$

Where the demagnetization factor $N = 0$ for the green (calculated) line.

3. THEORY

Coming from a very long rod in one axis, the magnetic field inside the rod will be derived. To use the internal field, it needs to be moved to the surface of the rod, which can be achieved by using cones (16), (17).

Before we start to derivate demagnetization factors, or look at the functioning of the Maxwell solver, we will look at the relation between J_s and the $\vec{H}$-field for different geometries. Starting with a cube, we will walk through the cases of a sphere and an ellipsoid. In all cases we assume, the magnetic field in our bodies is homogeneous.

3.1 ESTIMATE OF MAXIMUM FIELD OF AN INFINITE CUBE IN HALF SPACE

Let us assume a cube with $\begin{pmatrix} -\infty < x < \infty \\ -\infty < y < \infty \\ -\infty < z < 0 \end{pmatrix}$ and a magnetization of $\vec{M} = \begin{pmatrix} 0 \\ 0 \\ M_z \end{pmatrix}$ and calculate the field at the position $\vec{r} = \begin{pmatrix} 0 \\ 0 \\ \varepsilon^+ \end{pmatrix}$, by starting from the surface divergence of $\nabla \cdot \vec{B} = 0$ at $\vec{r} = \begin{pmatrix} 0 \\ 0 \\ 0 \end{pmatrix}$ and applying a Gaussian Pillbox (18) we obtain:

$$\vec{n} \cdot \vec{B}_{Out} = \vec{n} \cdot \vec{B}_{In} \tag{3.1}$$

Inserting $\vec{B} = \mu_0(\vec{H} + \vec{M})$ into (3.1), we obtain:

$$\vec{n} \cdot \mu_0(\vec{H}_{Out} + \vec{M}_{Out}) = \vec{n} \cdot \mu_0(\vec{H}_{In} + \vec{M}_{In}) \tag{3.2}$$

We know, the body is magnetized, but the air around it is not, so $\vec{M}_{Out} = 0$ and we also know from symmetry:

$$\vec{H}_{In} = -\vec{H}_{Out} \tag{3.3}$$

Inserting the argument (3.3) into equation (3.2) yields:

$$\vec{n} \cdot \mu_0 2\vec{H}_{Out} = \vec{n} \cdot \mu_0 \vec{M}_{In} \tag{3.4}$$

$$\vec{n} \cdot \mu_0 \vec{H}_{Out} = \vec{n} \cdot \mu_0 \frac{\vec{M}_{In}}{2} \tag{3.5}$$

Since $J_s = \mu_0|\vec{M}_{In}|$ we can produce a field of J_s with two magnets, when assuming the air gap separating them is infinite small.
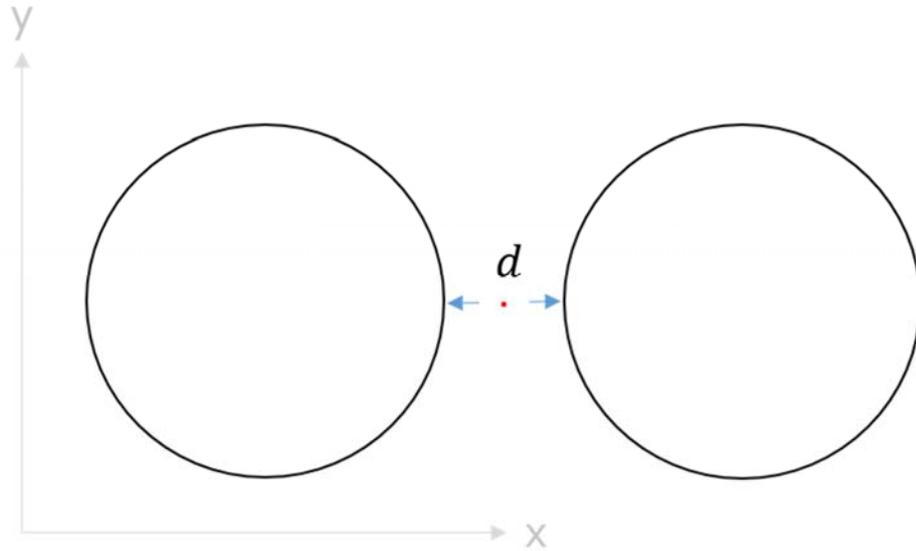
3.2 ESTIMATE OF MAXIMUM FIELD OF A SPHERE

FIGURE 1: TWO SPHERES, WITH AN INFINITE SMALL DISTANCE d BETWEEN THEM

When we change the form of the magnets to a sphere, we can calculate the simple dipole field of a single sphere outside the sphere using the expression of the dipole field (19). We now calculate the field at the boundary of the sphere where $r = a$ and in the direction of the magnetization. The vector $\vec{m}$ describes the magnetic moment (20):

$$\vec{B}(\vec{r}) = \frac{\mu_0}{4\pi} \left(\frac{3\vec{r}(\vec{m} \cdot \vec{r})}{r^5} - \frac{\vec{m}}{r^3} \right) \tag{3.6}$$

Since, we assume the vector of the magnetization is parallel to $\vec{r}$, we can write:

$$\vec{B}(\vec{r}) = \frac{\mu_0}{4\pi} \left(\frac{3\vec{m}}{r^3} - \frac{\vec{m}}{r^3} \right) = \frac{2\mu_0 \vec{m}}{4\pi} \tag{3.7}$$

When inserting $\vec{m} = \frac{4\pi a^3}{3} \vec{M}$ in to (3.7), and only looking in one direction $\left(\vec{M} = \begin{pmatrix} 0 \\ 0 \\ M_s \end{pmatrix} \right)$ with the use of $\mu_0 M_s = J_s$,

we can see:

$$B = 2\,\mu_0 \frac{M_s}{3} = \frac{2}{3} J_s \tag{3.8}$$

Which means, that for a measurement, in a gap of infinite small size between two spheres, we can expect a field of $\frac{4}{3} J_s$ – which is already above the value of J_s.

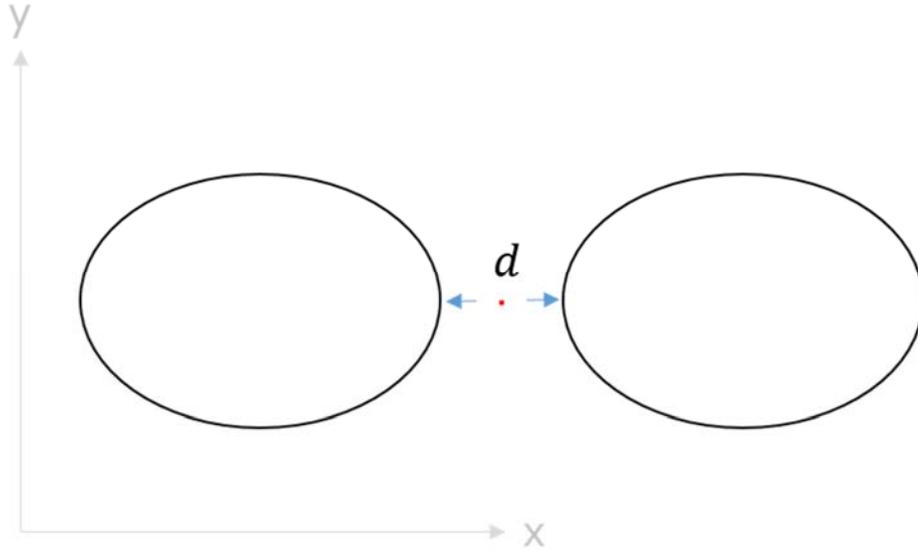## 3.3   ESTIMATE OF MAXIMUM FIELD OF ELLIPSOIDS

FIGURE 2: TWO ELLIPSOIDS, WITH AN INFINITE SMALL DISTANCE d BETWEEN THEM

We altered the form from a sphere to an ellipsoid, which is infinite stretched in the x-axis (which is also the direction of the magnetization). In the case of the ellipsoid we will distinguish the linear and the saturated situation.

3.3.1   LINEAR CASE

In the linear case we expect the χ to amplify the stray field outside of the body. Coming from (3.2) we write (using $\vec{H} = \vec{H}_{Ext} - \nabla u^{\pm}$):

$$\mu_0\big(\vec{H}_{Ext} - \nabla u^- - \vec{H}_{Ext} + \nabla u^+\big) \cdot \vec{n} = \mu_0\,\vec{M} \cdot \vec{n} \tag{3.9}$$

We now define:

$$(\nabla u^+ - \nabla u^-) \cdot \vec{n} = \vec{M} \cdot \vec{n} \tag{3.10}$$

as the jump condition on the boundary of our body and use the fact that the stray field inside of a body is defined by the negative magnetization multiplied by a demagnetization factor N. So, with:

$$-|\nabla u^+| = -NM \tag{3.11}$$

where $\vec{M}$ is defined as:

$$\vec{M} = \chi(\vec{H}_{Ext} - \nabla u^+) \tag{3.12}$$

and with (after rearranging (3.11) with the relation (3.12) for $\vec{M}$) we get:

$$\nabla u^+ = \frac{N\chi \vec{H}_{Ext}}{N\chi + 1} \tag{3.13}$$

Now we can use (3.12) again, and replace the $-\nabla u^+$ term with $-N\vec{M}$. This brings us to:

$$\vec{M} = \chi \vec{H}_{Ext} - N\vec{M}\chi \tag{3.14}$$

$$\vec{M} = \frac{\chi \vec{H}_{Ext}}{N\chi + 1} \tag{3.15}$$

Finally we are now able to insert (3.13) and (3.15) in to our jump condition and obtain an expression for $-\nabla u^-$:

$$\left(\frac{N\chi \vec{H}_{Ext}}{N\chi + 1} - \nabla u^- \right) \cdot \vec{n} = \left(\frac{\chi \vec{H}_{Ext}}{N\chi + 1} \right) \cdot \vec{n} \tag{3.16}$$

Simplified and rearranged this gives us an expression for the stray field outside of the body:

$$-\nabla u^- \cdot \vec{n} = \left(\frac{\chi \vec{H}_{Ext}(1 - N)}{N\chi + 1} \right) \cdot \vec{n} \tag{3.17}$$

Which means that for large χ the formula simplifies to $-\nabla u^- \cdot \vec{n} = \left(\frac{\vec{H}_{Ext}(1-N)}{N} \right) \cdot \vec{n}$. If we insert the value $N = \frac{1}{3}$ (for a sphere), we get $-\nabla u^- = 2\vec{H}_{Ext}$ for the stray field on the outside.

3.3.2 SATURATED CASE

Mathematically the case is pretty much the one from above, except we have to redefine (3.11) to:

$$-\nabla u^+ = -N\vec{M}_S \tag{3.18}$$

Where M_S indicates, the material is now in saturation and we left the linear area of the μ. Inserting (3.18) into our jump condition (3.10) yields:

$$-\nabla u^- = (1 - N)\vec{M}_S \tag{3.19}$$

For the indefinitely stretched ellipsoid in the x-axis the N becomes 0 and with two ellipsoids we can achieve a stray field outside of the body of two times the $\vec{M}_S$.

$$-\nabla u^- = 2\vec{M}_S \tag{3.20}$$

3.4 FLUX CONCENTRATION

To utilize the just derived magnetic field for a real application, the amplified magnetic field must be brought to the vicinity of the rod – because obviously we measure and work with magnetic fields outside the body. This can be achieved by using flux concentrators. As this thesis will show, the angle of these flux concentrators is critical for success or failure.

We will use the so called gain-factor (G) to describe the enhancement of the field. The gain factor is used in many papers to describe amplifying effects for magnetic fields ((17), (21), (22), (23)). The idea is, that a perfectly shaped cone will increase the field on the surface of its tip.

In our approach, we will consider a long rod and no air gap. In the following we consider the rod as a body of second degree which is a simplification but it is required for the derivation as given in ref. (24). A body of second degree has to fulfill the following mathematical condition:

$$\vec{x} = \begin{pmatrix} x \\ y \\ 1 \end{pmatrix} \qquad Q = \begin{pmatrix} A & B & D \\ B & C & E \\ D & E & F \end{pmatrix} \qquad \vec{x}^T Q \vec{x} = 0 \qquad\qquad (3.21)$$

If a uniform external magnetic field H_{Ext} is applied to an isotropic, linear and homogenous material with a high permeability (μ_0), the magnetic field $\vec{H}$ inside the material can be amplified. We can describe the magnetic flux density $\vec{B}$ in relation to $\vec{H}$ as follows:

$$\vec{B} = \mu_0(\vec{H} + \vec{M}) = \mu_0(1 + \chi)\vec{H} \qquad\qquad (3.22)$$

μ_0 is the vacuum permeability and $\vec{M}$ is the magnetization of the material. When combining the external and internal field in the probe (by simply adding them up), we obtain:

$$\vec{H} = \vec{H}_D + \vec{H}_{Ext} \qquad\qquad (3.23)$$

$\vec{H}_D$ (or $-\nabla u$) can be set into relation to $\vec{M}$ in the direction of every axis with the help of a demagnetization factor N. This demagnetization factor is a purely geometric influence. For a more detailed description of the N factor, continue with the papers of J. Osborne (13) and J. C. Maxwell (24). This allows us to set the geometry into relation with the material, as χ is material dependent only. For $i = x, y, z$ we can write:

$$(H_D)_i = -N_i M_i \qquad\qquad (3.24)$$

And therefore, when inserting the relation in the equation above, we obtain:

$$H_i = (H_{Ext})_i - N_i \chi H_i \qquad\qquad (3.25)$$

where χ is now a value which is determined by the used material. Paul Leroy et al. 2006 (17) showed, that small magnetic fields can be amplified by a factor of 1000 and more, if the relative permeability of the used material is high enough. This is due the fact, that if the soft magnetic material used for operation is used far below its saturation point (in the linear area), the small change of $\vec{H}$ results in a big change of $\vec{B}$ (see the red area in the graph below) – but: always consider that every material is saturated at a certain point, and μ is of nonlinear nature in every part of the hysteresis.
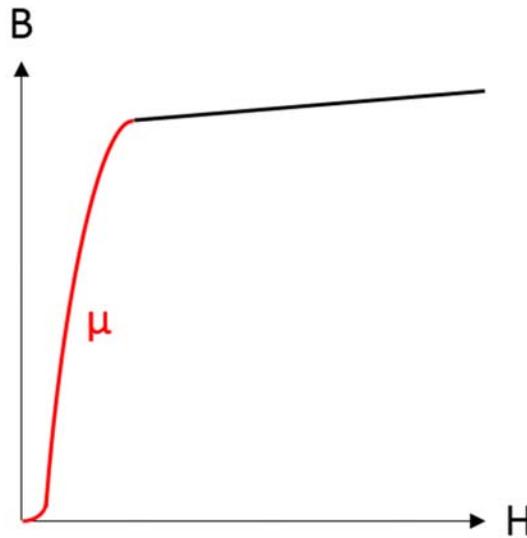
Some values for permeability and saturation for some ferromagnetic materials (25):

TABLE 1: TYPICAL VALUES FOR SOME FERROMAGNETS AND AIR

Material	Relative Permeability $\left({}^{\mu}/_{\mu_0}\right)$	Saturation [T]
Air	~ 1	
Nickel	$100 - 600$	0.4
Ferrite	16 – 640	0.2 – 0.5
Electric Steel	4 000	1.6 – 1.8
Iron (99.8%)	5 000	1.6 – 2.2
Mu-Metal	20 000	0.8

We start with an equation describing the relation between internal field, external field and demagnetization factor and rewrite it (we still only operate in the linear area of μ), until we end up with a formal expression for the field along one axis.

$$H_i = (H_{Ext})_i - N_i \, \chi H_i \tag{3.26}$$

$$H_i(1 + N_i \, \chi) = H_{Ext} \tag{3.27}$$

$$\frac{1}{(1 + N_i \, \chi)} = \frac{H_i}{H_{Ext}} \tag{3.28}$$

$$\frac{\mu}{\mu_0} \frac{1}{(1 + N_i \, \chi)} = \frac{\mu}{\mu_0} \frac{H_i}{H_{Ext}} \tag{3.29}$$

$$\frac{\mu_r}{(1 + N_i \, \chi)} = \frac{B_i}{B_o} \tag{3.30}$$

$$\frac{B_0 \mu_r}{(1 + N_i \chi)} = B_i \tag{3.31}$$

Here one has a first explanation for the amplification at hand: A high μ_r increases the maximum field linearly, while a big value for the demagnetization factor N_i decreases the amplification almost linearly.

With $\chi = (\mu_r - 1)$ we can rewrite formula (3.31):

$$\frac{\mu_r}{(1 + N_i (\mu_r - 1))} = \frac{B_i}{B_o} \tag{3.32}$$

For $\mu_r \gg 1$ (in the red part of the hysteresis plot) the formula can be simplified to:

$$\frac{B_i}{B_o} = \frac{1}{N_i} \tag{3.33}$$

With the obtained results, it looks like a very small demagnetization factor N_i could do the trick in tremendous amplifications – but always keep in mind, that close to J_s the value of μ_r becomes almost 1 and therefore the amplification does not really work anymore.

To get an idea on the magnitudes of this demagnetization factor, again see the papers of J. A. Osborn (ellipsoids, (13)) and A. Aharoni (prisms, (12)). Well known examples are an infinite plate ($N_x = 1$), a sphere $\left(N_x = \frac{1}{3}\right)$, or a cylinder of infinite length ($N_x \to 0$).

If we want to know the gain of a magnetic field by using the cones we can make a simple assumption, thanks to the magnetic flux conservation theorem. For a cone with the closed surface S_1 and the closed cone tip surface S_2, one finds different values for B in this cone at the base and at the tip.
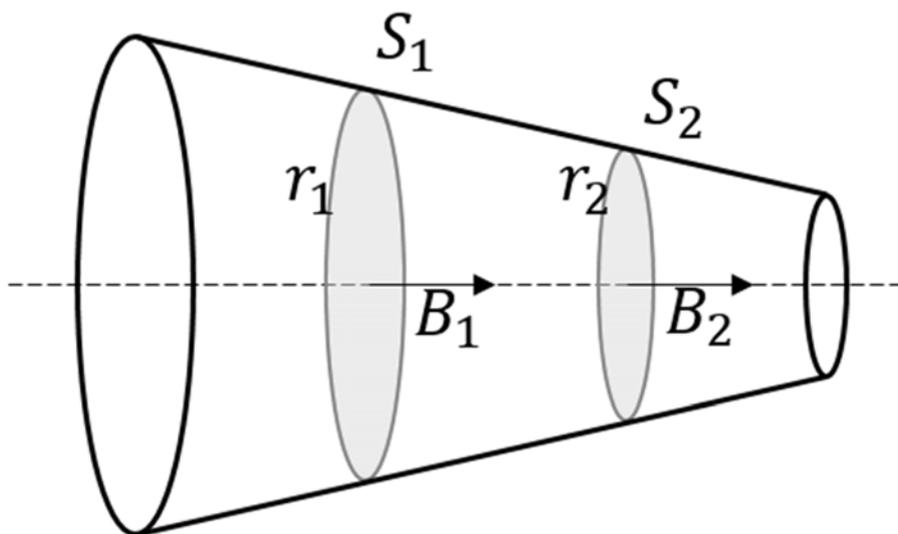

FIGURE 3: CONE SHAPED FLUX CONCENTRATOR

We can describe the magnetic flux integrated over the closed surfaces using the following relation:

$$B_1 S_1 = B_2 S_2 \qquad (3.34)$$

$$B_1 = \frac{S_2}{S_1} B_2 \qquad (3.35)$$

$$\frac{B_1}{B_0} = \frac{S_2}{S_1} \frac{B_2}{B_0} \qquad (3.36)$$

One can now introduce the gain factor (G) at this point (as described at the beginning of this chapter). It is simply defined by the magnetic induction B over the induced magnetic induction B_0. Furthermore the surface integrals yield all the same terms, but the radius of the surface which alters the equation to (where F/I be the final and initial fields):

$$G_F = G_I \frac{r_2^2}{r_1^2} \qquad (3.37)$$

3.5 MAXWELL EQUATIONS FOR FEMME USAGE

The particular used method is a subclass of the FEMME package, developed by Dr. Florian Bruckner in his PhD thesis (26). For a detailed explanation of how the Maxwell solver exactly works, further study of his thesis is strongly recommended. The first thing we take a look at now, will be the Maxwell equations inside the body, then we head over to describe the problem outside of the body and combine it with the jump conditions at the boundary – which will provide us with a suitable method of calculating occurring fields.

3.5.1 INSIDE THE BODY

Let us take a look at a magnetic field strength *H* which consists of two parts in entire space: The external field strength H_{Ext} which is produced by electric currents outside of the magnet and the stray field produced by the magnetization of the magnet: $-\nabla u$.

$$\vec{H} = \vec{H}_{Ext} - \nabla u \qquad (3.38)$$

With the knowledge of the Maxwell equation $\nabla \cdot \vec{B} = 0$ and the basic magnetic field relation $\vec{B} = \mu^+ \vec{H}$, we obtain:

$$\vec{B} = \mu^+ (\vec{H}_{Ext} - \nabla u) \qquad (3.39)$$

which we combine with the Maxwell equation $\nabla \cdot \vec{B} = 0$, leading us to:

$$\nabla \cdot \left(\mu^+ (\vec{H}_{Ext} - \nabla u) \right) = 0 \qquad (3.40)$$

Which in a linear case for μ yields:

$$\nabla \cdot \vec{H}_{Ext} = \Delta \cdot u \qquad (3.41)$$

In general the μ can be in the non-linear regime of the virgin curve – this means the value for μ^+ has to be solved by iteration, because it is position dependent.

3.5.2 OUTSIDE THE BODY

Coming from (3.41) and taking into account that outside of the body $\mu = \mu^-$ we obtain,

$$\mu^- \nabla \cdot \vec{H}_{Ext} = \Delta \mu^- \cdot u \qquad (3.42)$$

The external applied magnetic field H_{Ext} is produced by current which implies that H_{Ext} can be expressed as:

$$\vec{H}_{Ext} = \nabla \times \vec{A} \qquad (3.43)$$

Where $\vec{A}$ is a scalar vector potential which can be written as $\vec{A}(\vec{r}) = \frac{\mu^-}{4\pi} \int d^3 r' \frac{\vec{J}(\vec{r})}{|\vec{r} - \vec{r}'|}$. Hence, we can calculate the divergence of the external field as,

$$\nabla \cdot \vec{H}_{Ext} = \nabla \cdot \left(\nabla \times \vec{A}\right) = 0 \tag{3.44}$$

$$\Delta \cdot u = 0 \tag{3.45}$$

Which leaves us with the homogeneous Poisson equation, also called Laplace equation. Unlike simpler cases, we do not know the polarization of the material, which means we are dealing with an open boundary problem.

3.5.3 BOUNDARY JUMP CONDITIONS

At the surface of a body (remember the pill box and basic electrodynamics), we can compare the fields inside and outside the body (this time using the normal vectors $\vec{n}$). For the sake of readability we now again introduce μ^+ and μ^- for μ outside and inside the body. μ^- obviously is the same thing as μ_0.

$$\vec{n} \cdot \left(\vec{B}_{out} - \vec{B}_{in}\right) = 0 \tag{3.46}$$

$$\vec{n} \cdot \left(\mu^+ \vec{H}_{Ext} - \mu^+ \nabla u^+ - \mu^- \vec{H}_{Ext} + \mu^- \nabla u^-\right) = 0 \tag{3.47}$$

$$\vec{n} \cdot \left(\vec{H}_{Ext}(\mu^+ - \mu^-)\right) = \vec{n} \cdot \left(\nabla(\mu^+ u^+ - \mu^- u^-)\right) \tag{3.48}$$

When introducing the normal derivative of the potential at the surface of the magnetic part $\left(\Phi = \frac{\partial u}{\partial n}\right)$, we can write:

$$\vec{n} \cdot \left(\vec{H}_{Ext}(\mu^+ - \mu^-)\right) = \mu^+ \Phi^+ - \mu^- \Phi^- \tag{3.49}$$

We furthermore claim, that u is continuous everywhere:

$$u^+ - u^- = 0 \tag{3.50}$$

The only thing we know (and are able to use) is the material behavior. Or as you might want to call it: The hysteresis of the material (see chapter "Iron-cones") for an actual hysteresis of our working material). For simpler handling, we only used the virgin curve of the material.
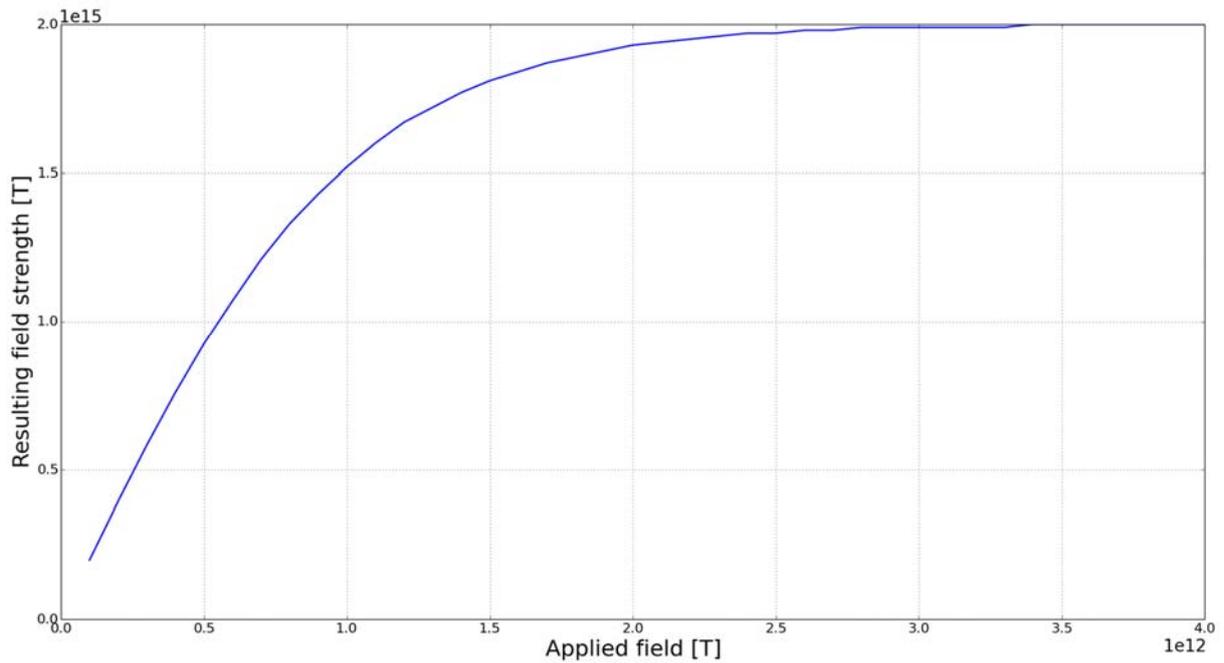
GRAPH 6: VIRGIN CURVE OF THE MAGNET INTERPOLATED FROM FEMME

On a numerical base, we end up solving this equation – where $H_{Ext} - \nabla u$ is a value of the function μ. At the start of every iteration we only know H_{Ext} exactly.

$$\vec{B} = \mu(\vec{H}_{Ext} - \nabla u) \cdot (\vec{H}_{Ext} - \nabla u) \tag{3.51}$$

When we combine equations (3.40), (3.45), (3.49) and (3.50), we can solve (3.51) in iterative steps, like the graphic beneath suggests. This is due to the fact, that this set of four equations have one solution for a given μ and $\vec{H}_{Ext}$.
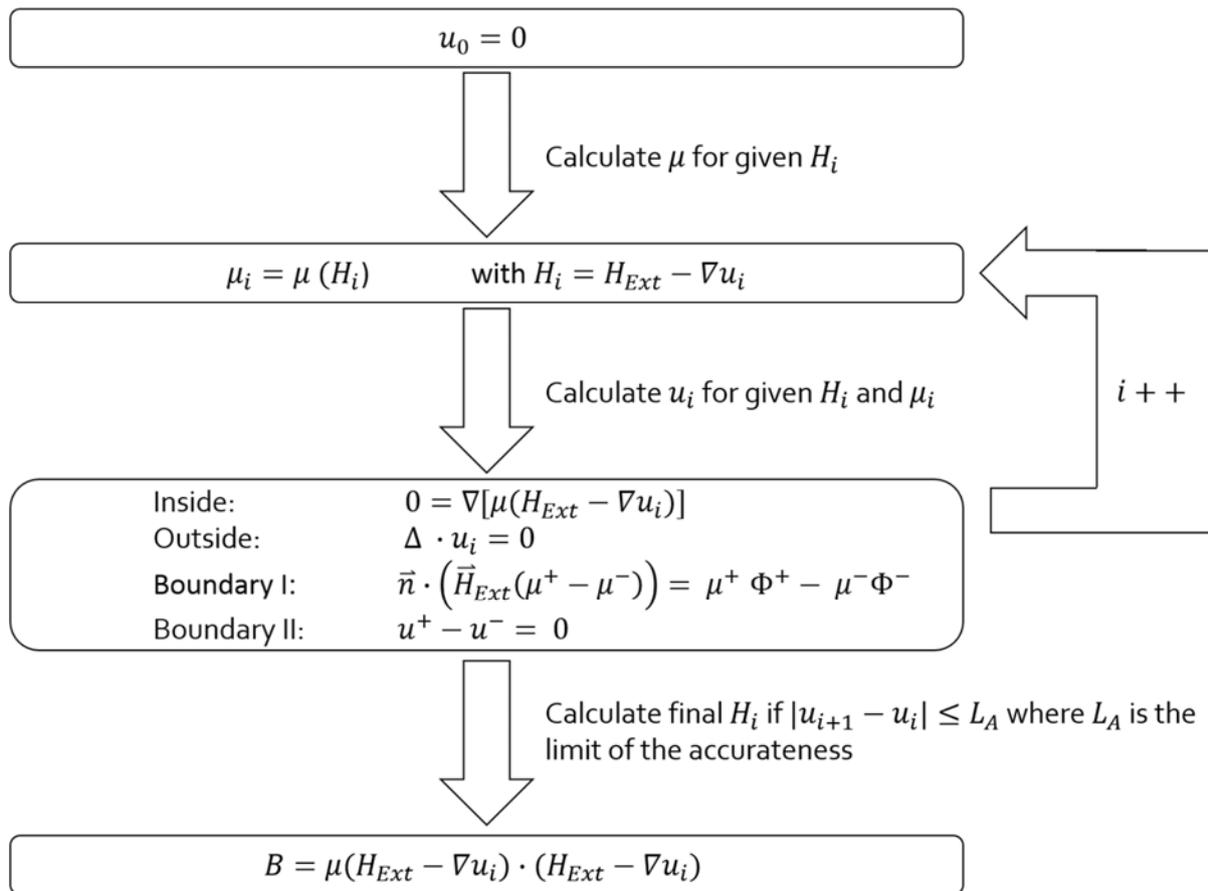
$$u_0 = 0$$

Calculate μ for given H_i

$$\mu_i = \mu\,(H_i) \qquad \text{with } H_i = H_{Ext} - \nabla u_i$$

Calculate u_i for given H_i and μ_i

$i + +$

Inside: $\qquad 0 = \nabla[\mu(H_{Ext} - \nabla u_i)]$
Outside: $\qquad \Delta \cdot u_i = 0$
Boundary I: $\qquad \vec{n} \cdot \left(\vec{H}_{Ext}(\mu^+ - \mu^-)\right) = \mu^+ \, \Phi^+ - \mu^- \Phi^-$
Boundary II: $\qquad u^+ - u^- = 0$

Calculate final H_i if $|u_{i+1} - u_i| \leq L_A$ where L_A is the limit of the accurateness

$$B = \mu(H_{Ext} - \nabla u_i) \cdot (H_{Ext} - \nabla u_i)$$

FIGURE 4: ITERATION STEPS TO CALCULATE $\vec{B}$

Figure 4: Iteration steps to calculate $\vec{B}$ describes the working schematic of the Maxwell solver in a very simple way. More information can be found here: (26), (27).

3.6   Finite Elements Method

"In mathematics, the finite element method (FEM) is a numerical technique for finding approximate solutions to boundary value problems for differential equations. It uses variational methods (the calculus of variations) to minimize an error function and produce a stable solution. Analogous to the idea that connecting many tiny straight lines can approximate a larger circle, FEM encompasses all the methods for connecting many simple element equations over many small subdomains, named finite elements, to approximate a more complex equation over a larger domain." (28)

FEM nowadays is a standard tool at the hands of an engineer, therefore only a short overview about the method will be given. For deeper understanding, the following references are suggested: (29), (30), (31), (32).

For simplicity we will introduce the basic concepts of FEM for the Poisson Equation $\Delta u = f$. If we now multiply the Poisson Equation with a so-called test function v and integrate it over a region Ω. For simpler handling, a 1 dimensional case is described, using $f = \nabla \cdot M$. The described method is called FEM-BEM coupling, for more information the paper of J. Fetzer et al. is a valuable source (33).

$$\int_\Omega \Delta u \, v \, dr = \int f \, v \, dr \qquad (3.52)$$

We claim this equation to be valid for every v restricted to the Sobolev space H_0^1 which is 0 on the boundary $\partial\Omega$. When applying integration by parts on (3.52) we get:

$$\int_\Omega \nabla u \cdot \nabla v \, dr = \int_\Omega f v \, dr + \int_{\partial\Omega} \vec{n} \, \nabla u \, v \, ds \qquad (3.53)$$

which we can simplify to the following equation, if one claims that $v = 0$ (Dirichlet boundary conditions (34)) on the boundary:

$$\int_\Omega \nabla u \cdot \nabla v \, dr = \int_\Omega f \, v \, dr \qquad (3.54)$$

Here, the equation is in its weak form, but still must not have any jumps. Coming from (3.54) we can define a number of ϕ_i basis functions, which relate to u_h with (which limits our choice of v to the $v_h \in V_h$, where V_h is the finite dimensional function space).

$$u_h = \sum_i u_i \, \phi_i \qquad (3.55)$$

In its discretized form, (3.54) shows as:

$$\int_\Omega \nabla u_h \cdot \nabla v_h \, dr = \int_\Omega f \, v_h \, dr \qquad (3.56)$$

Where the ϕ_i functions come from the continuous Galerkin functions (or so-called Hat-functions) as seen in the graphic below.
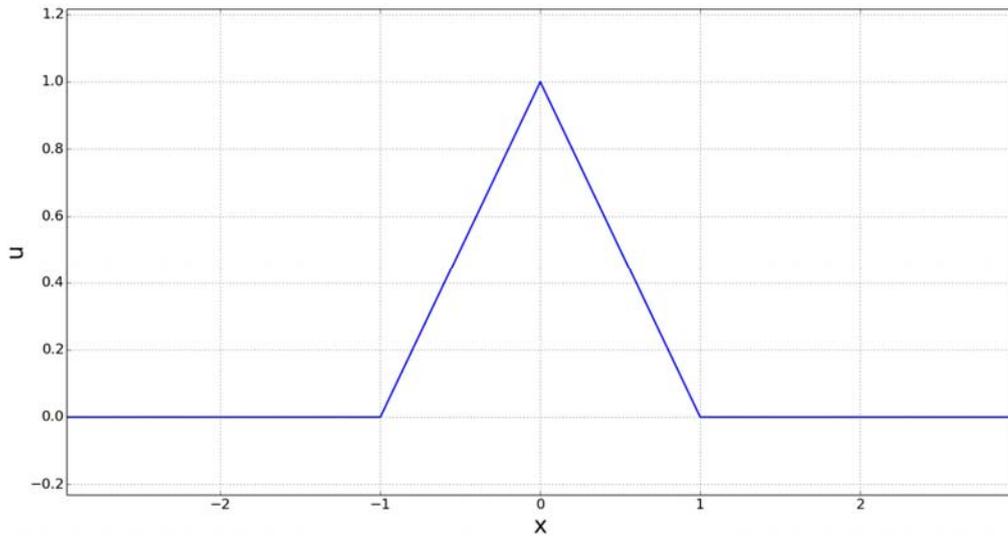
GRAPH 7: FIRST ORDER HAT FUNCTION

Each hat function is defined to have value 1 at a single node, value 0 at all other nodes and is piecewise linear and globally continuous (from a value 1 node to a neighbor node the function decreases to 0 on both sides – see Graph 7: First order hat function). We can now combine equations (3.54) and (3.55) to obtain the form (and due to the nature of the hat function only get non-zero results, for neighboring nodes):

$$\sum_{i=1}^{N} u_i \int_{\Omega} \nabla \phi_i \cdot \nabla \phi_j = \int_{\Omega} f \, \phi_j \tag{3.57}$$

And introduce the so-called stiffness matrix $A_{ij} = \int \nabla \phi_i \cdot \nabla \phi_j$. We now have to solve the equation system for each value j (where N is the number of nodes) in order to obtain the unknown coefficients u_i:

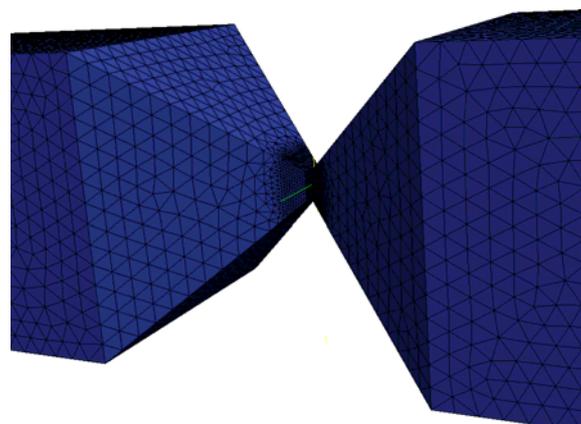$$\sum_i u_i A_{ij} = f_j \qquad \forall j \, (j \dots N) \tag{3.58}$$

FIGURE 5: NON-LINEAR MESH OF A QUADRATIC CONE

4. TOOLS

The three ingredients for a finite element simulation are usually a software to draw objects, a meshing software for acquiring an actual mesh and a third software, capable of using the mesh in order to calculate with it. In this project all of this was combined using python, to script the simulations on the server.

4.1 SALOME

The models were drawn using this free software (35). For better results the parts were split apart into separate models on various positions to be able to enhance the mesh quality in more important areas (an overall increased meshing quality would have led to an enormous long time for simulating). Furthermore Salome has a very powerful python export function, which leaves the user with only a few lines of code, to generate models and mesh them.

Version used: 7.3.0 on Windows 8 $x64$ and Ubuntu 12.04 $x64$

4.2 NETGEN

The parts were then meshed using the NETGEN library (36), developed by Joachim Schöberl from Johannes Kepler University Linz. NETGEN is an automatic 3d tetrahedral mesh generator which is already included in the Salome package and therefore easy to use, with the GUI version of Salome and the server installation, which can be programmed using the Python interface.

After a Salome server was installed, python scripts were built around these codes to vary the variable parts of the geometry.

Version used: 5.1 (comes with the Salome installation)

4.3 FEMME

The meshed models were plugged into FEMME, a FEM software designed to calculate magnetic fields in given geometries (11). The software was fed with only the geometry and some material parameters. In our case, the most interesting material parameter is J_s. It directly describes the power of a magnet and the capability of the soft magnetic material (for example iron) to be magnetized.

In the simulation itself the field was evaluated using a virtual field box ($0.2 \times 0.2 \times 0.2\ mm$ of size), which is a kind of a simulated Hall probe – meaning: This is where the magnetic field is "measured". We evaluate the field of the soft magnet and the hard magnet within the box. As Maxwell's equations are additive, we just need to sum up the resulting values for an overall field. This is the field a Hall probe would measure at this position.

Version used: 5.0.10

5. SIMULATION RESULTS

5.1 FLUX CONCENTRATORS IN THE LINEAR REGIME

FEMME does not only allow to simulate hard and soft magnetic materials attached to each other, but also a material exposed to an applied field. This is an interesting point, when we think about a GMR (Giant Magneto Resistance) sensor, and how we can increase very small fields for proper measurements (37). Beyond the point where μ comes close to the value 1.0 (in other terms: we have to stay on the red line of the hysteresis chart once again), the amplification effect disappears due to the saturation of the soft magnetic material.

In this part, different fields way above the ones a state-of-the-art magnet can supply were applied on a geometry, which is close to one used at Infineon.
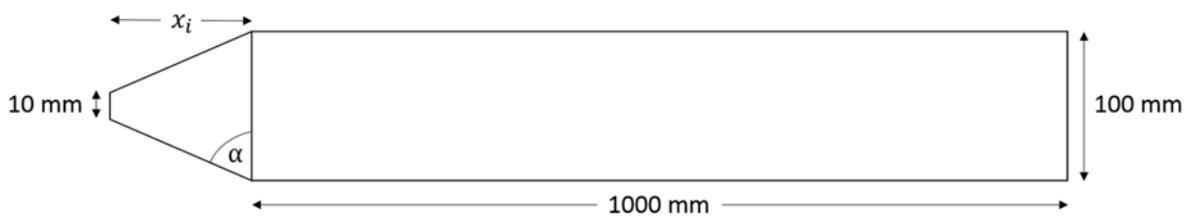
FIGURE 6: SKETCH OF THE SIMULATED FLUX CONCENTRATOR

These flux concentrators for the sensors are approximately 100 times smaller than the one sketched in Figure 6: Sketch of the simulated flux concentrator, but also the gap size will decrease by the factor 100 when comparing the results of the simulation with the real ones – so basically they equal out. The tip size (shown with $10\ mm$ in the drawing) was not altered here, because the sensor needs to be of that size at its tip due to some technological aspects, when they are built. The x_i value was altered in many iterations and with the knowledge of its value α is easy to calculate (where L_M is the height of the magnet – in this case $100\ mm$ – and R_C is the radius of the cone tip – here: $10\ mm$):

$$\alpha = \frac{180}{\pi}\arctan\left(\frac{x_i}{\frac{L_M}{2} - 2\ R_C}\right)$$

(5.1)

Fields of the following sizes were applied: $0.4\,, 0.2\,, 0.1\,, 0.05$ and $0.01\ T$.
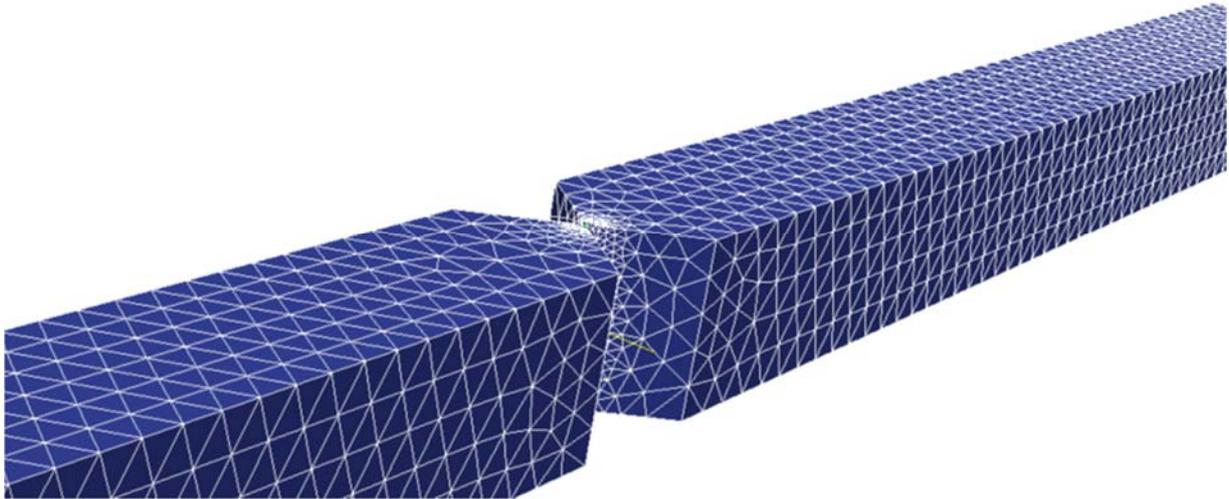
FIGURE 7: MESH OF THE SENSOR ARRANGEMENT

The following table shows the maximum achieved values, with some restrictions: The smaller the fields one wants to measure are, the closer the tip angle α converges to 90 ° - basically meaning, the cone tip grows massively in length. Especially the $0.05\,T$ and $0.01\,T$ fields are too weak for a small angles. If the angle was too small, a value for $\alpha = 73$ ° is given (the angles smaller than 73 ° always yield smaller fields).
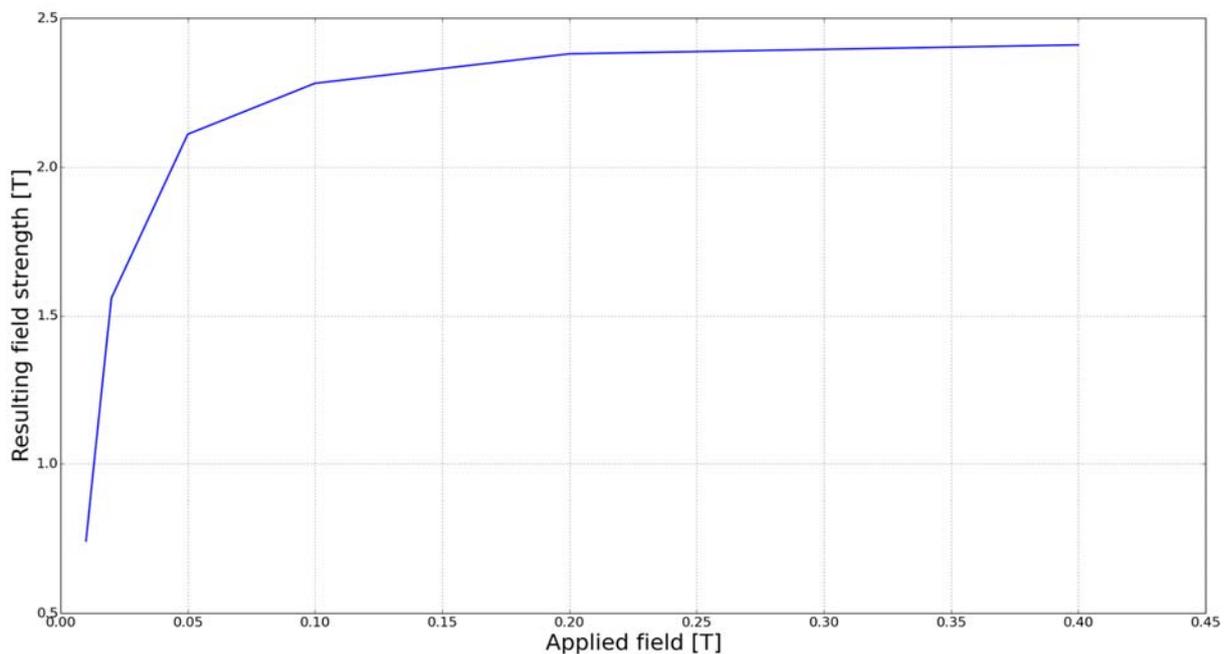
GRAPH 8: FIELD AMPLIFICATION FOR SMALL FIELDS

In this graph, the saturation of the iron is once again visible – it has a shape similar to the ones in Graph 16: Hysteresis of the used iron with a law-of-approach fit and Graph 17: Hysteresis of the used iron (annealed) with a law of approach fit, (38).

5.2   FLUX CONCENTRATORS IN SATURATION
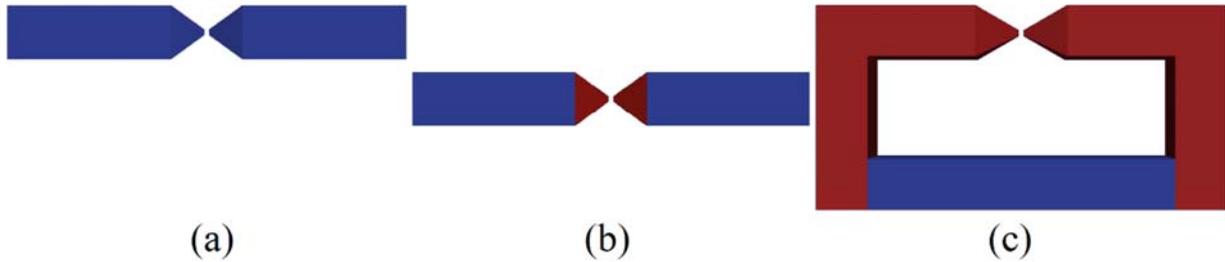
The following three geometries were simulated:

FIGURE 8: SHAPES OF THE SIMULATED BODIES. RED PARTS ARE SOFT MAGNETIC, BLUE PARTS ARE HARD MAGNETIC

a)   Two hard magnetic cones

b)   Two hard magnets (shown in blue color) with attached soft magnetic cones (shown in red color)

c)   A soft magnetic yoke (shown in red) with cones attached to a magnet (shown in blue color)

To show the importance of J_s, the simulation was made with two different values for the soft magnetic (shown in red) parts of the bodies: $J_s = 1.43\,T$ (which is a typical value for a good $Nd_2Fe_{14}B$ (28) magnet) and for $J_s = 2.0\,T$ (normal quality iron). In all three cases the magnet was $30 \times 30 \times 60\,mm$ (two magnets), or $30 \times 30 \times 120\,mm$ (one magnet). The cones are always quadratic and the tip is very small, compared to the size of the magnets: $0.3 \times 0.3\,mm$.
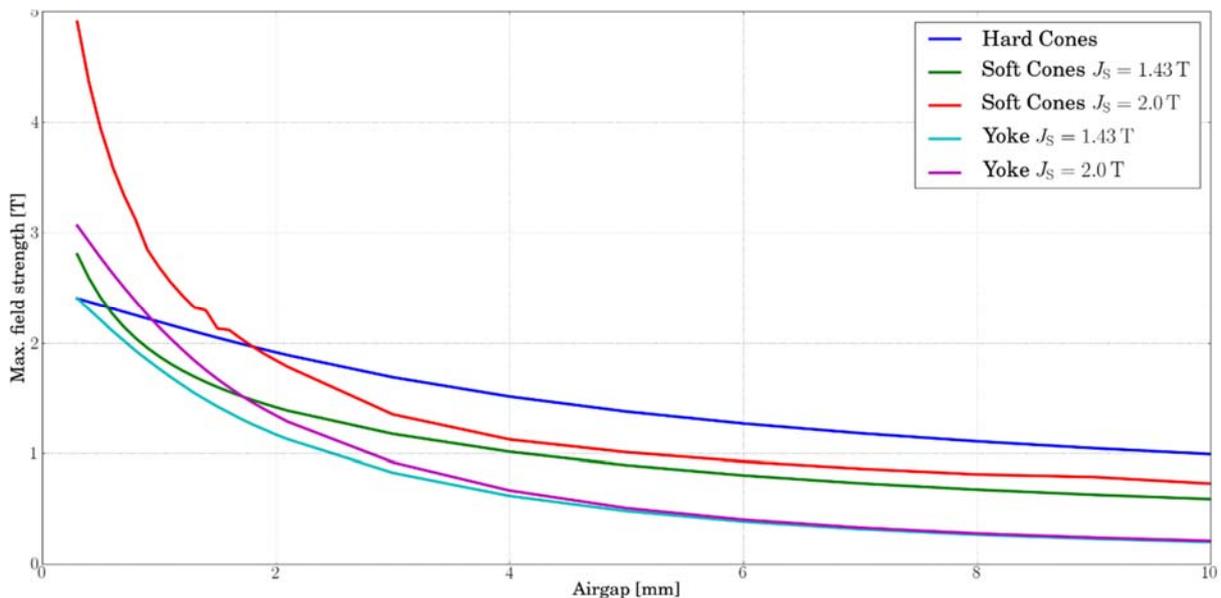
GRAPH 9: COMPARISON OF THE MAXIMUM FIELDS AT A PERFECT CONE ANGLE FOR INCREASING AIR GAPS

The figure above shows the maximum values for the best cone angle α as shown in chapter "Materials". Until a gap size of 1.8 mm there is a big advantage when one tries to amplify the magnetic field with a soft magnetic material of a higher J_s. The usage of a yoke is according to this simulations of no practical use (also it is harder to build), as a simple soft magnetic cone does the job better.

The following four pages show all results from the simulations. The colored lines always show the field strength for a certain angle, the black line always indicates the maximum value that was achieved. For a better comparison the following table offers an overview for maximum values in an easy-to-read table. The values at 0.5 , 1.0 and $2.0\ mm$ only were are shown to prove, that there is no perfect angle for every arrangement, even with an increased gap size. From every gap size only the angle which yielded the maximum field is printed in the table. The other values can be taken from the graphs.

TABLE 2: HAND PICKED AIR GAPS AND THE CORRESPONDING FIELDS

Type	Air gap [mm]	Cone height [mm]	Maximum field [T]	Angle at max. field [°]
Hard cones (a)	0.5	15.0	2.34	48.0
	1.0	14.0	2.19	46.0
	2.0	11.0	1.91	39.2
Soft cones: $J_s = 1.43\ T$ (b)	0.5	10.0	2.41	36.5
	1.0	9.0	1.88	33.7
	2.0	8.0	1.42	30.7
Soft cones: $J_S = 2.0\ T$ (b)	0.5	9.0	3.93	33.7
	1.0	7.0	2.69	27.4
	2.0	5.0	1.84	20.3
Yoke: $J_s = 1.43\ T$ (c)	0.5	12.0	2.21	41.6
	1.0	12.0	1.77	41.6
	2.0	18.0	1.17	53.1
Yoke: $J_s = 2.0\ T$ (c)	0.5	15.0	2.78	48.0
	1.0	16.0	2.14	49.8
	2.0	29.0	1.34	65.0

Unlike suggested in some literature, simulations do not suggest there is something like a perfect angle. The book of a famous magnetism researcher for example suggests 54.7 ° for a yoke to be the perfect fit (16). Also, the angle of 45 ° is not always a good shot – in our case the 45 ° would result in a cone height of about 13.5 mm – which is not ideal in many cases. The table also shows the following trends:

a)   With increasing gap size, the angle (α) with the maximum field is getting smaller

b)   A higher J_s results not only in an increasing field, but also in a smaller angle (α)

5.2.1 SINGLE PLOTS FOR THE DIFFERENT CASES

In order to understand, where the numerical fluctuations of the maximas are coming, one has to keep in mind, that less than 30 different cones are simulated for each setting usually (in some cases some simulations were redone in other areas, because the effect was beyond the usual cone sizes used in the other simulations). So the descrete values may not always be at the best position. To adress this issue, a 9th order polynomial fit was layed over the results in order to get a smoother plot. Altough this works just fine for curves with a clear maxmium, even this enhanced method can easily fail, when the values are not that much distinguishable. This does not only happen, when the angles where the maximum field is achvied are very big (so the cones are very long), but also when some numerical fluctuation occur.

5.2.1.1 HARD CONES (CASE (A))

FIGURE 9: COMPLETE HARD MAGNETIC MATERIAL
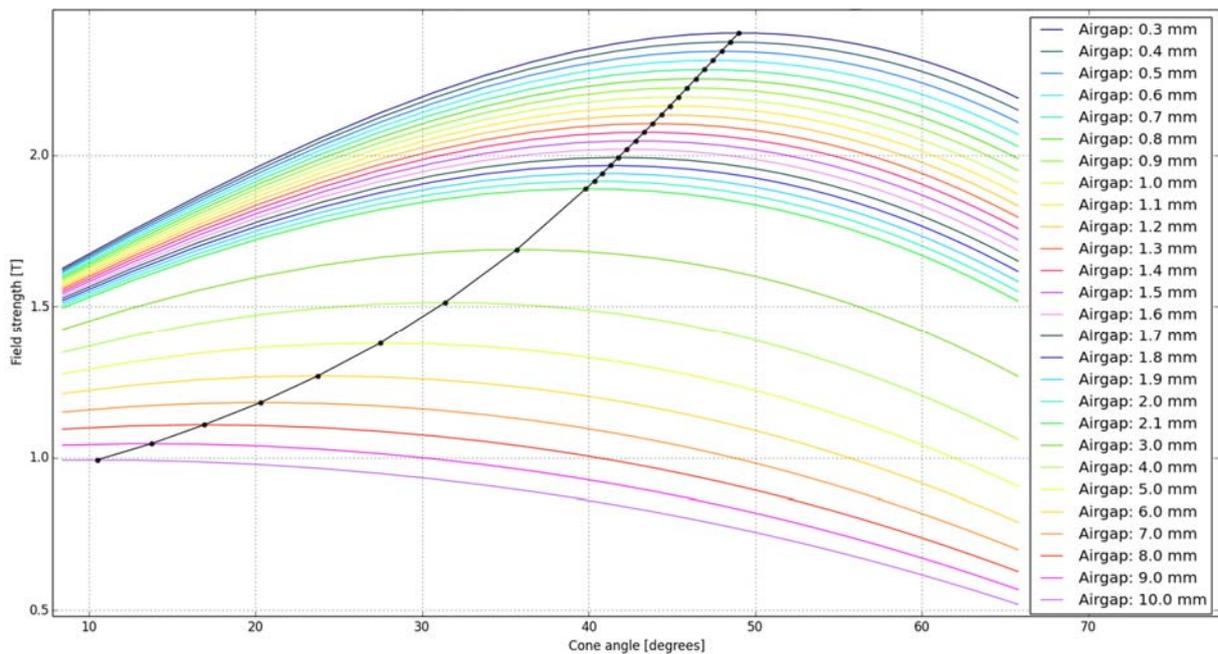

GRAPH 10: HARD CONES IN THEIR MAXIMUM FIELDS

The straight forward case, with no mentionable fluctuations. Decreasing the gap size leads to a higher field, the angle at which the higher field is achieved is higher for larger gaps.

S<small>OFT CONES (CASE (B) – WITH</small> $J_s = 1.43\,T$)

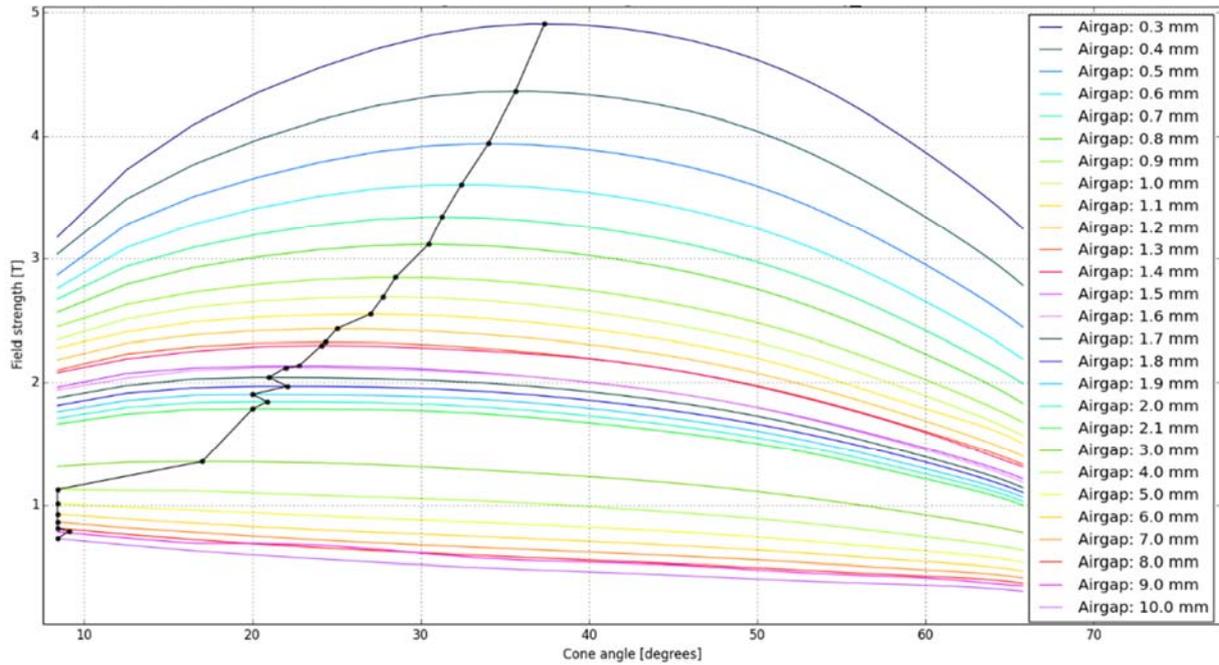FIGURE 10: HARD MAGNETIC MATERIAL (BLUE) WITH SOFT MAGNETIC (RED) CONES

GRAPH 11: SOFT MAGNETIC CONES AND THE CORRESPONDING MAXIMUM FIELDS FOR IRON OF POOR SATURATION
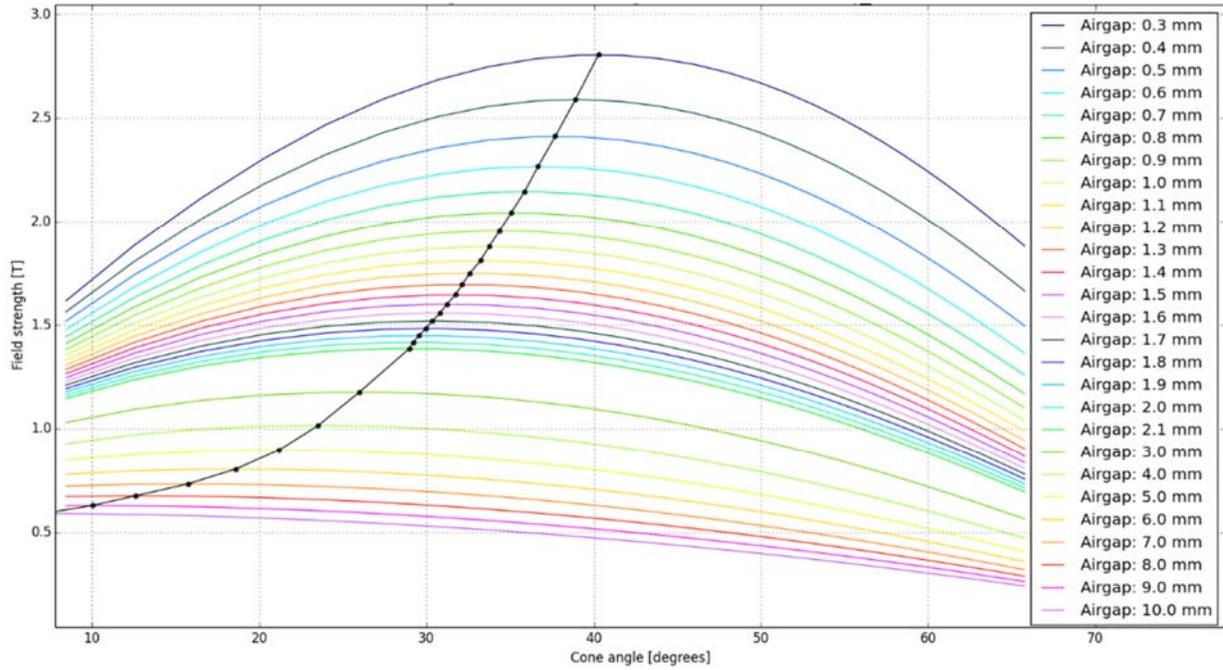
More numerical fluctuations, but still very much in line with our former assumptions.

5.2.1.3 Soft cones (case (b)) – with $J_s = 2.0\,T$

FIGURE 11: HARD MAGNETIC MATERIAL (BLUE) WITH SOFT MAGNETIC (RED) CONES

GRAPH 12: SOFT MAGNETIC CONES AND THE CORRESPONDING MAXIMUM FIELDS FOR IRON OF HIGH SATURATION

More numerical fluctuations, the bigger the air gaps become, the less effect the cone has. The fluctuations in the middle are again of numerical nature, as one can imagine the shape of a smooth line in this graph.
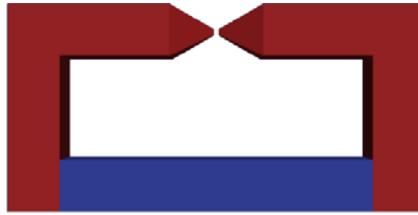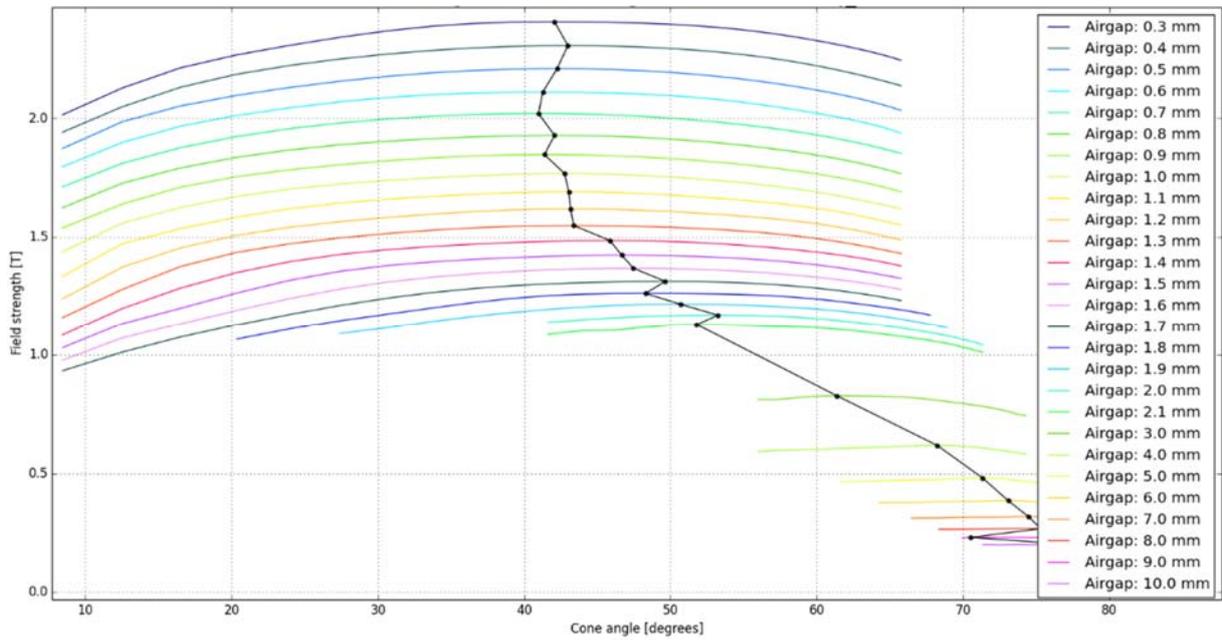
Yoke (case (c) – with $J_s = 1.43\,T$)

FIGURE 12: SOFT MAGNETIC YOKE (RED) WITH A HARD MAGNET (BLUE) BENEATH

GRAPH 13: YOKE WITH SOFT MAGNETIC CONES AND THE CORRESPONDING MAXIMUM FIELDS FOR IRON OF POOR SATURATION

Even more numerical fluctuations, the bigger gaps have their maximum above a cone height of $30\,mm$ (where the simulation usually stops). Extra data was produced in a second simulation, but it is getting harder to see an actual trend. The usage of air gaps above a gap size of $3.0\,mm$ is questionable.

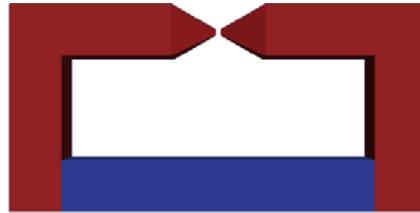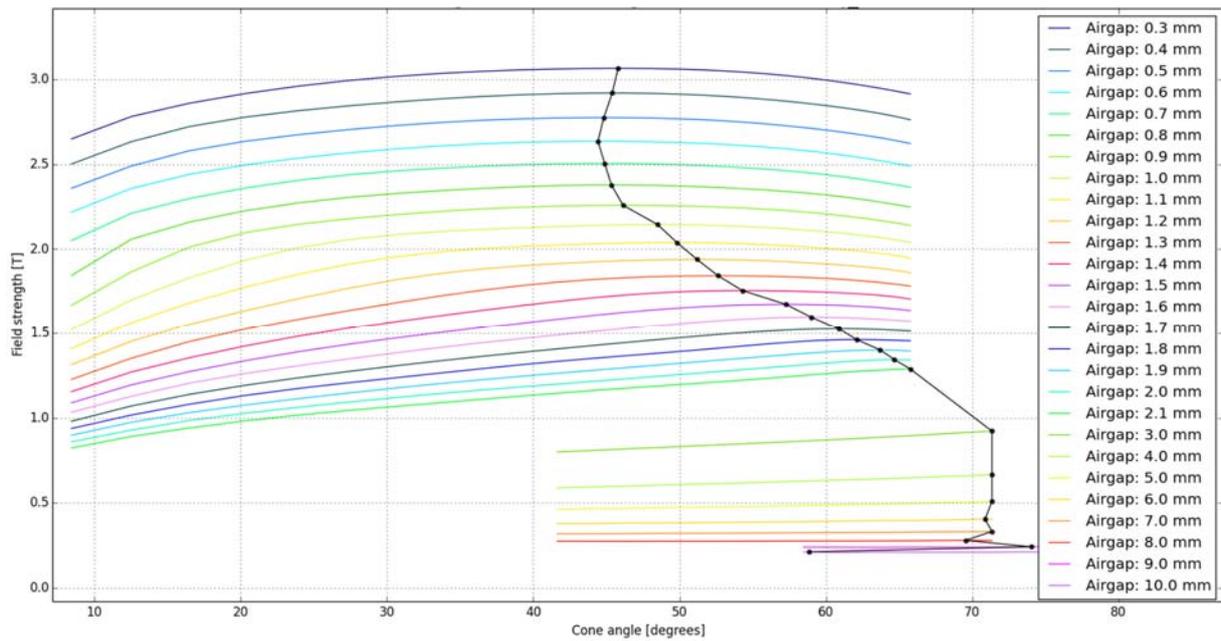YOKE (CASE (C) – WITH $J_s = 2.0 \, T$)

FIGURE 13: SOFT MAGNETIC YOKE (RED) WITH A HARD MAGNET (BLUE) BENEATH

GRAPH 14: YOKE WITH SOFT MAGNETIC CONES AND THE CORRESPONDING MAXIMUM FIELDS FOR IRON OF HIGH SATURATION

A clear trend can be seen until a gap size of about $2.0 \, mm$. Bigger gaps lead to a very chaotic behaviour of the calculation of the maximum values.

6. Experimental Setup

In experiments the well controllable conditions a simulation can offer vanish, and a new geometry had to be chosen, which had a suitable size for a practical measurement. The cones were altered from a quadratic basal plane to a circular shape (because it is easier to turn such a part than to mill it) and magnets already bought for an older project were reused. To get comparable results, the arrangement built at Vienna University of Technology's workshop was simulated again, this data can be found under "Simulating the Experiment".

6.1 Materials

The basic schematic is shown beneath. Through the variation of the cone height (x) the angle α was altered. Two of these are facing each other as it is shown in the first chapter. The field is measured at the point P, as described in the chapter "Sensor".
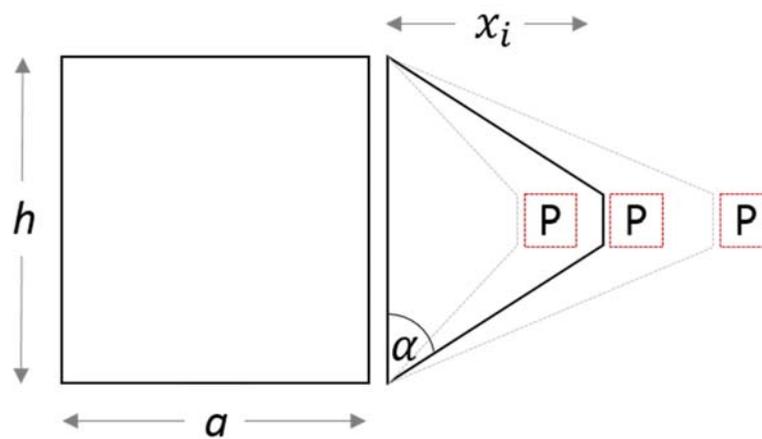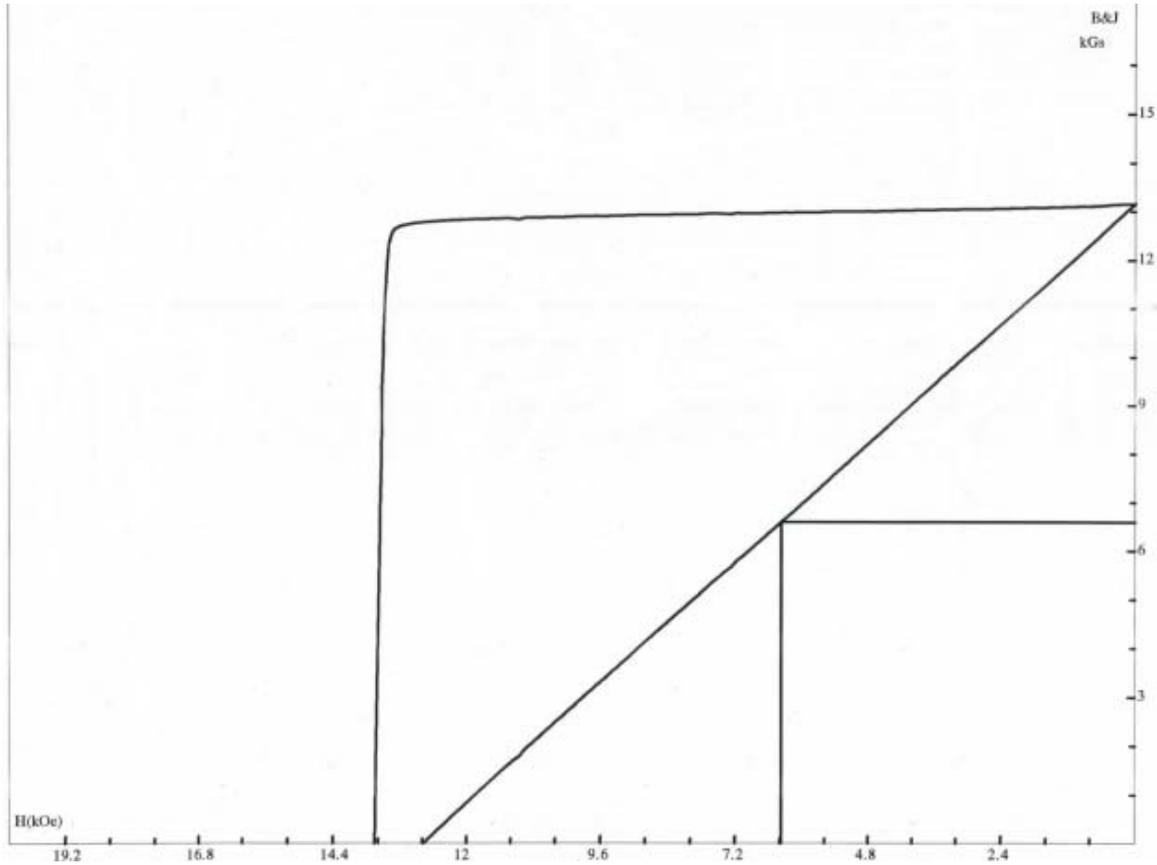

FIGURE 14: DIMENSIONS OF THE MILLED CONES

The quadratic part of the drawing shows the magnet, while the variable cone formed geometry refers to a soft magnetic material – in this case iron.

6.1.1 NᴅFᴇB-ᴍᴀɢɴᴇᴛs

The magnets used in the experiment were obtained from supermagnete.de (39). The size of the magnets is $a \times a \times h$ with a being $40.0\ mm$ and h being $a/2$. On each side of the retaining device two of the magnets were stacked together, before they were attached to the cones. So the overall size of the magnets was $40.0\ mm$ in every dimension.

GRAPH 15: WORKING POINT OF THE MAGNET

The size of the magnets can also be obtained from the drawing (see chapter "Materials" - Figure 14: Dimensions of the milled cones), the demagnetization factor is approximately 0.5 by calculation (12), (40).

TABLE 3: BASIC DATA OF THE $Nd_2Fe_{14}B$ MAGNETS

Material	$Nd_2Fe_{14}B$
Coating	Ni
Production type	Sintering
Curie temperature	$310\ °C$
Adhesive force	$588\ N$
Magnetic remanence	$1.29 - 1.32\ T$
Coercivity bHc	$860 - 955\ kA/m$
Coercivity iHc	$318 - 334\ kJ/m^3$

6.1.2 IRON-CONES

The cones consist of a high quality ARMCO standard iron (41), which was milled into form from the Vienna University of Technology workshop. See the reference for more data on the iron: (42).

The workgroup of Prof. Roland Grössinger helped with creating a hysteresis of the working material. It was important to measure the exact saturation of the material, to feed the simulation with suitable numbers. In order to create those hysteresis loops, a ring (see Figure 15: Cut out ring for hysteresis measurement) was cut out and measured in the described method (43). The form of the ring is close to a donut, which means, that N becomes a neglectable factor for the measurement.

FIGURE 15: CUT OUT RING FOR HYSTERESIS MEASUREMENT

The simulation itself however was only fed with the data from the maximum saturation, not the hysteresis itself (which would have been possible, but more work). This is not of big importance, because the simulation proofed, the cone tips are saturated on the tip (surface). Therefore the most important value is the J_s value itself.

From this material multiple cones were milled, which were then smoothened to a plain surface with an asperity of $100 \, \mu m$ to reduce the air gap between the soft and hard magnetic materials. The cone radius at P varies between $0.2 \, mm$ and $1.8 \, mm$.
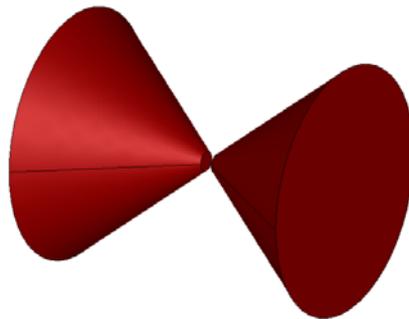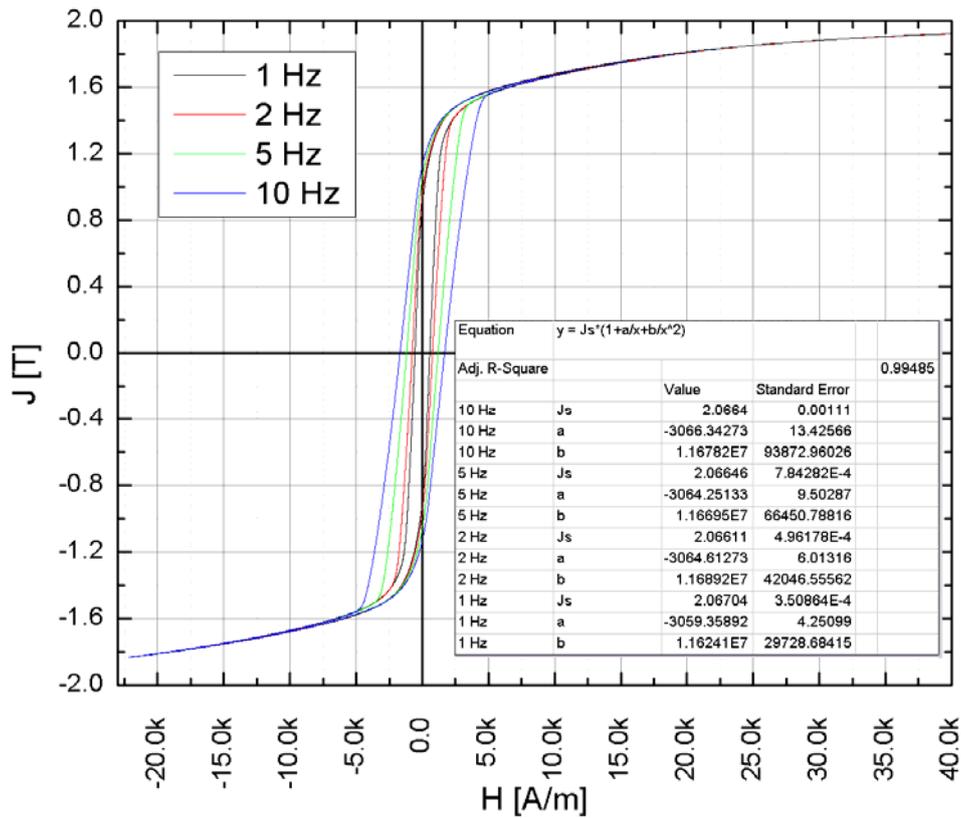

FIGURE 16: SKETCH OF THE CONES FOR THE EXPERIMENT

The sizes of x_1, x_2 and x_3 are $5.0 \, mm$, $14.0 \, mm$ and $25.0 \, mm$ which results in α being $20.5 \,°$, $44.0 \,°$ and $60.5 \,°$.

Usually iron saturates at around $2.0 \, T$. This value was also used for the simulation, but was not 100% accurate, as the hysteresis measurement revealed (44).

GRAPH 16: HYSTERESIS OF THE USED IRON WITH A LAW-OF-APPROACH FIT

The most important value for the simulation is the J_s value on $10, 5, 2$ and $1 \ Hz$, which indicates, the iron has a very little higher saturation then the simulation used ($2.066 \ T$ in the measurement versus $2.0 \ T$ in the simulation). The iron ring needed more than $6.2 \ m$ of wire to be wrapped around it for a proper measurements.
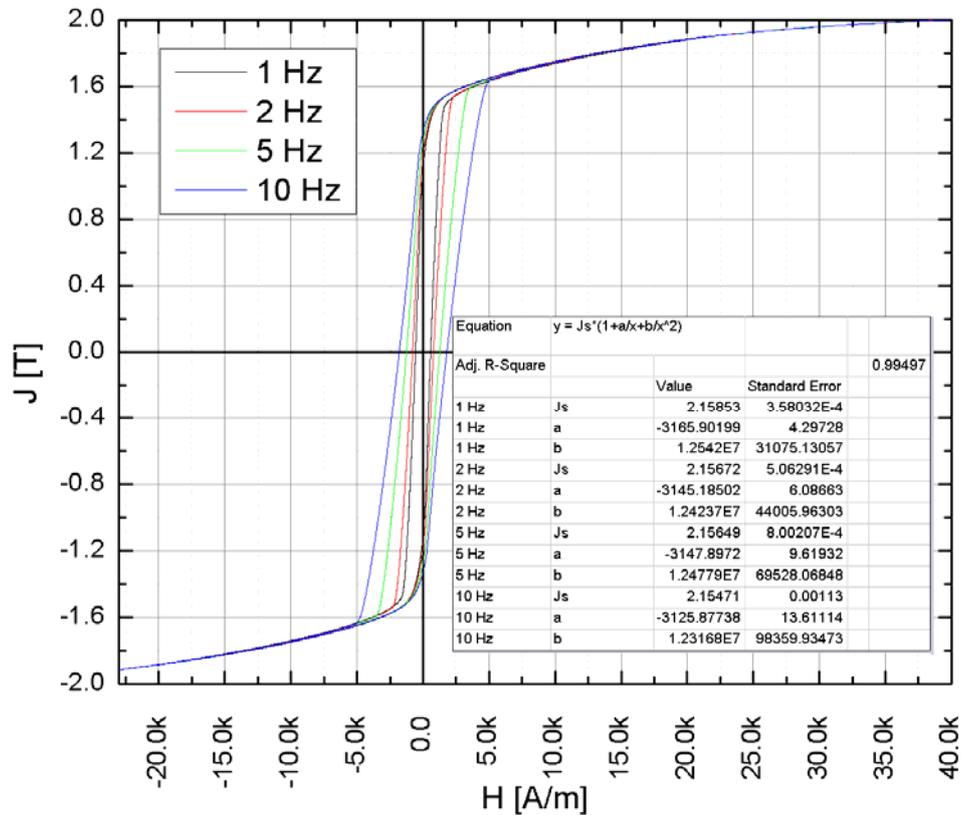
GRAPH 17: HYSTERESIS OF THE USED IRON (ANNEALED) WITH A LAW OF APPROACH FIT

Comparison of Graph 16: Hysteresis of the used iron with a law-of-approach fit and Graph 17: Hysteresis of the used iron (annealed) with a law of approach fit show, that after annealing the iron increases the J_s by about 4 %. This is due to the fact, that the annealed iron is easier to saturate and therefore easier to measure with the used law of approach method (38) - J_s itself is a constant. See the references to the ARMCO iron for further details (41). The important value on 10, 5, 2 and 1 Hz has increased due to the annealing to $J_s = 2.15\ T$.

With the law of approach, the saturation magnetization is obtained by extrapolating $\vec{H} \to \infty$. For further information on the law of approach fit, see the related references: (45), (38).
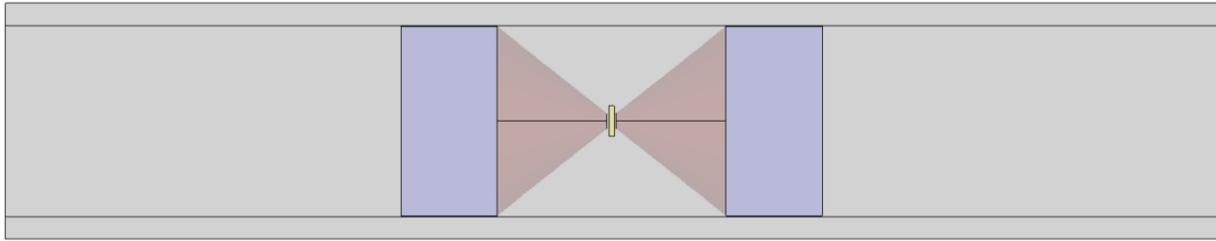
6.1.3   RETAINING DEVICE FOR THE MAGNETS

FIGURE 17: EXPERIMENTAL SETUP FOR MEASURING THE FIELDS

The pipe (shown in grey color) is a quadratic tube with space for the cones and the magnets milled out. It is built from a non-magnetic material (plastic). Hence the measured field is not influenced by the restraining device. Also the magnets are held in the correct position and therefore do not touch the sensor.
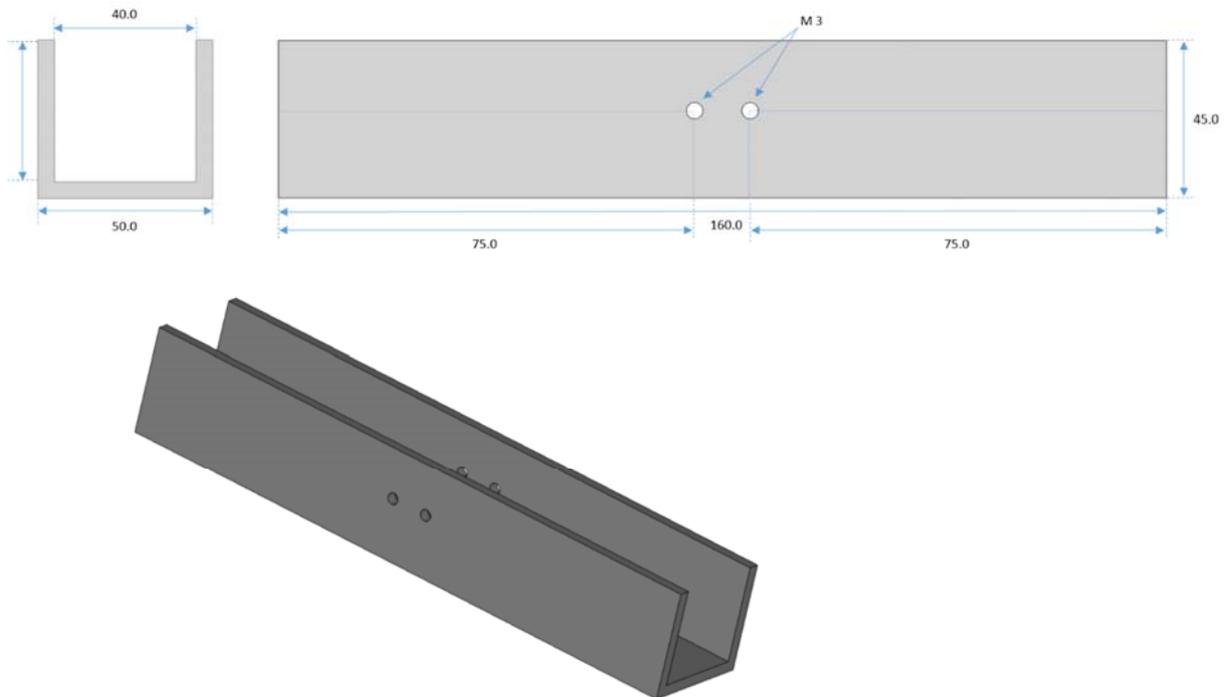

FIGURE 18: SKETCH AND DIMENSIONS OF THE RETAINING DEVICE

The sketch above was drawn for the Vienna University of Technology workshop.

6.2 SENSOR

Measuring magnetic fields is a standard problem in modern technology and nowadays many different kinds of sensors exist (46). For the experiment, a Hall sensor was used, because it is available on demand and it is easy to handle. A Hall sensor makes use of the effect with the same name, the Hall Effect (see chapter "Theory of a Hall sensor"). This effect occurs, if an orthogonal magnetic field interferes with a thin metallic layer, which carries current from one end to the other. It was first discovered by Edwin Hall in his PhD Thesis in 1879 (47). In circuit diagrams the Hall sensor is usually described by this electronic symbol:
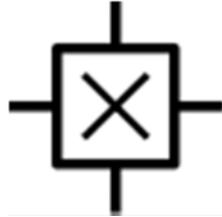

FIGURE 19: ELECTRIC SYMBOL OF A HALL SENSOR

According to the datasheet, $85.2\ mV$ measured on the multimeter would indicate a field of $1.0\ T$ – so we would need about $\sim 200\ mV$ on the screen of the multimeter, to beat the magnetic field above J_s.

TABLE 4: DATASHEET OF THE HHP-MU SENSOR BY AREPOC

Parameter	Unit	At 295 K
Nominal control current I_n	mA	10.0
Maximum control current I_c	mA	12.0
Sensitivity at I_n	mV/T	85.2
Offset voltage at I_n	μV	-15
Input resistance	Ω	30.0
Output resistance	Ω	25.0
Linearity error up to $1\ T$	%	≤ 0.5
Change of sensitivity due to reversing of the magnetic field	%	≤ 1.0
Operating Temperature range	K	$270 - 330$
Active area dimension	μm	$100\ \times 100$
Overall dimension $(w\ \times l\ \times h)$	mm	$2.3 \times 3.5 \times 0.63$

The Sensor has four wires:

TABLE 5: COLOR SCHEMATICS OF THE HHP-MU SENSOR

Color	Polarity	Use for
Green	Plus	Control current I_c
Black	Minus	Control current I_c
Red	Plus	Hall wire
Orange	Minus	Hall wire

The hall voltage U_H is generated at the red wire.

6.2.1   THEORY OF A HALL SENSOR

Electrons, ions or even holes carrying the electric current are influenced by any magnetic field which is applied (assuming it is not applied perfectly parallel). This force is called the Lorentz force, and it keeps the particles from following the shortest (straight, line of sight) line from one end of the conductor to another. This path becomes curved due to the perpendicular component of the applied magnetic field, creating a potential on the surface (on one side, more current carrying particles occur, which creates a scarcity on the other side).
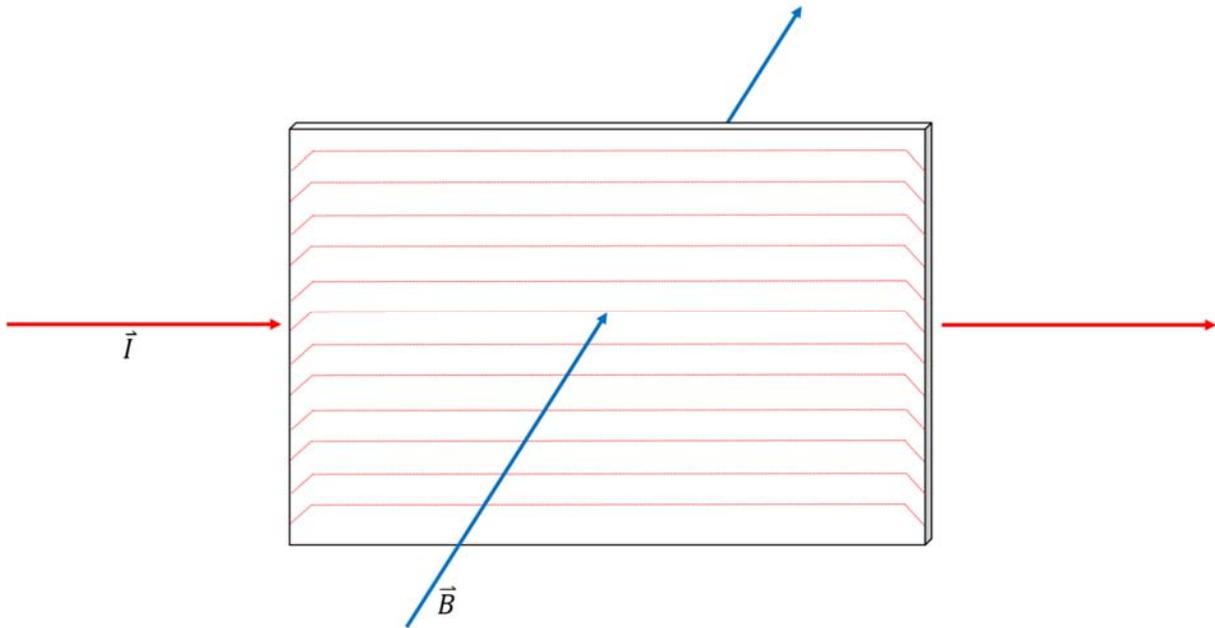

FIGURE 20: A MAGNETIC FIELD INFLUENCES THE CHARGE CARRYING PARTICLES

This potential is in relation to the amplitude of $\vec{B}$ and therefore a perfect way to measure it. For a simpler approach, we will not discuss temperature dependencies on the Hall Effect here.
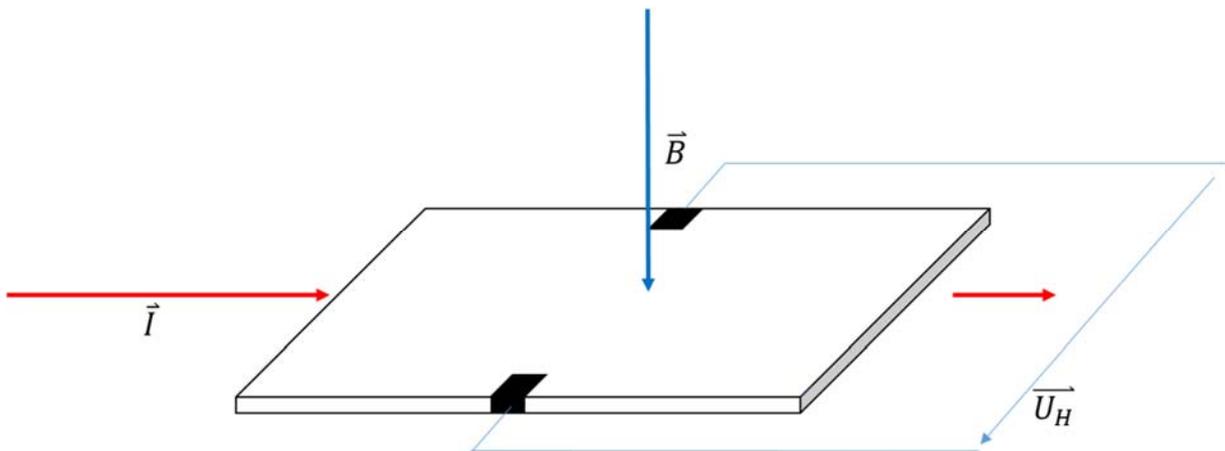

FIGURE 21: MEASUREMENT OF THE HALL VOLTAGE

Particles carrying a current, moving in a magnetic field feel a Lorentz force (where $\vec{v}$ is the drifting velocity of the electrons, q the charge of the conductor and $\vec{F}$ the Lorentz force):

$$\vec{F} = q\vec{v} \times \vec{B} \tag{6.1}$$

When a magnetic field is applied, an electronic field establishes, which compensates the sidetracking effect from the magnetic field. We can write:

$$q(\vec{E} + \vec{v} \times \vec{B}) = 0 \tag{6.2}$$

If we assume, that the current carrying particles only move along the x-axis, and the magnetic field $\vec{B}$ only has a z component. Or in short: $\vec{v} = \begin{pmatrix} v_x \\ 0 \\ 0 \end{pmatrix}$ and $\vec{B} = \begin{pmatrix} 0 \\ 0 \\ B_z \end{pmatrix}$, we can rewrite (6.2) to:

$$E_y - v_x B_z = 0 \tag{6.3}$$

When introducing $\vec{J}$ as the current density, which is defined by: $\vec{J} = nq\vec{v}$ and rewriting (6.3):

$$E_y = \frac{1}{nq} j_x B_z = A_H j_x B_z \tag{6.4}$$

where $\frac{1}{nq} = A_H$ is the Hall-Constant, which characterizes the size of the Hall Effect.

For simpler handling we will now assume, that the conductor we are describing is a parallel plate capacitor. This is a justified assumption, because we started with a normal conductor and separated the currents in it. So every current carrying particle feels the same Lorentz Force and we have a homogenous electrical field. In such a capacitor, the $\vec{E}$ field is linked to the voltage by the relation (b is the width of the capacitor):

$$E_y = \frac{U_H}{b} \tag{6.5}$$

We rewrite $\vec{j_x}$ as $j_x = \frac{I}{bd}$, where I is the electric current, and b describes again the width and d the thickness of the capacitor. This rewriting allows us to find a very simpler expression for the Hall-Voltage U_H which only depends on measurable quantities:

$$U_H = \frac{A_H B_z I}{d} \tag{6.6}$$

So, reshaped for B_z (6.6) reads as:

$$B_z = \frac{U_H d}{I A_H} \tag{6.7}$$

6.2.2 IMPLEMENTATION OF THE HALL SENSOR

For measuring maximal fields, the cones need to be as close as possible to each other, therefore an as small as possible probe was needed. After some research on the web, the Hall sensor HHP-MU by the company AREPOC (Bratislava) was chosen (48). Its small overall dimensions make it ideally suited for space-limited applications. This probe is partially protected by a resin enclosure, but the electrical system remains uncovered.

The distance between the surface of the active area and the probe's upper surface is $150 \ \mu m$. Overall dimensions are $2.3 \times 3.5 \times 0.63 \ mm$. It was connected to a constant power source of $2o$ mA and the readings were read out using a digital standard multimeter.
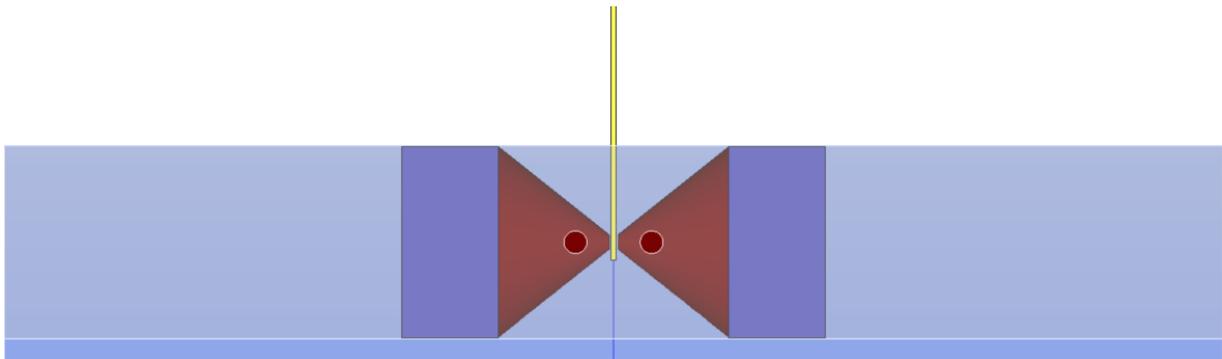

FIGURE 22: HALL SENSOR BETWEEN THE CONES

The sensor is in no physical contact with the cones and can measure up to $30 \ T$ at room temperature. For more information about the sensor, see the reference (48).

For getting real measurments a constant current source was built, which provided the hall sensor with its control current I_C. The constant current source was also built within the Vienna University of Technology and applied a constant current of $11 \ mA$ to the sensor.
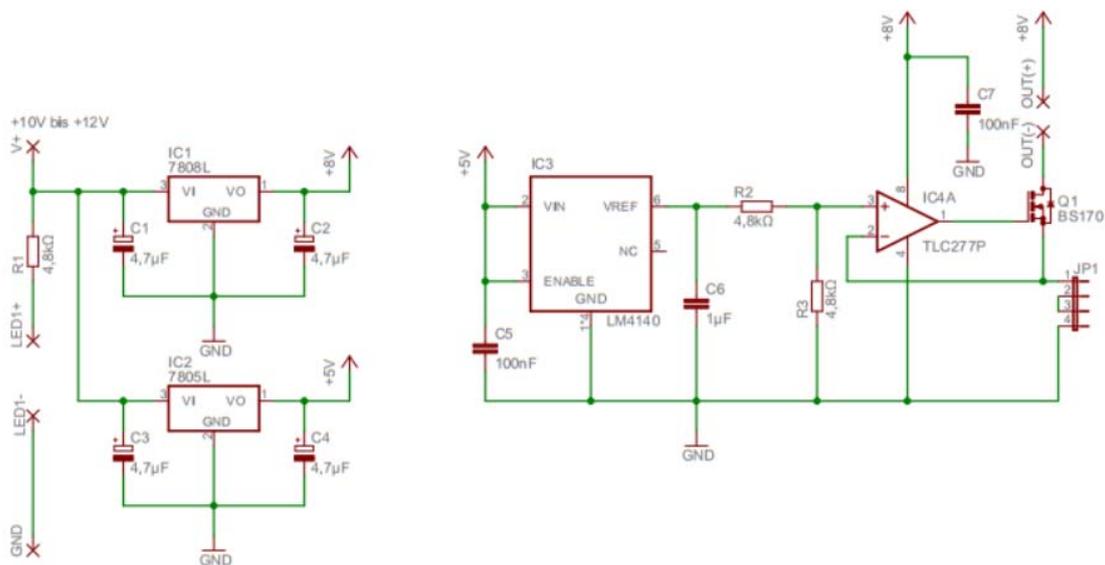

FIGURE 23: SCHMEATICS OF THE CONSTANT CURRENT SOURCE

7. SIMULATING THE EXPERIMENT

As mentioned in the "Materials" chapter, another simulation was done. At this point we already had an idea of type (soft cones) and material (obviously a high quality iron), but did not know the influence of the tip radius. This simulation showed, that there is not only a perfect cone angle for every problem, but also a perfect tip size for a certain cone. The dummybox evaluated in this simulation was $0.2 \times 0.2 \times 0.2 \; mm$ of size. An air gap size of *1.0* mm was chosen, as a good trade-off between a high field and enough room to operate with a hall sensor.
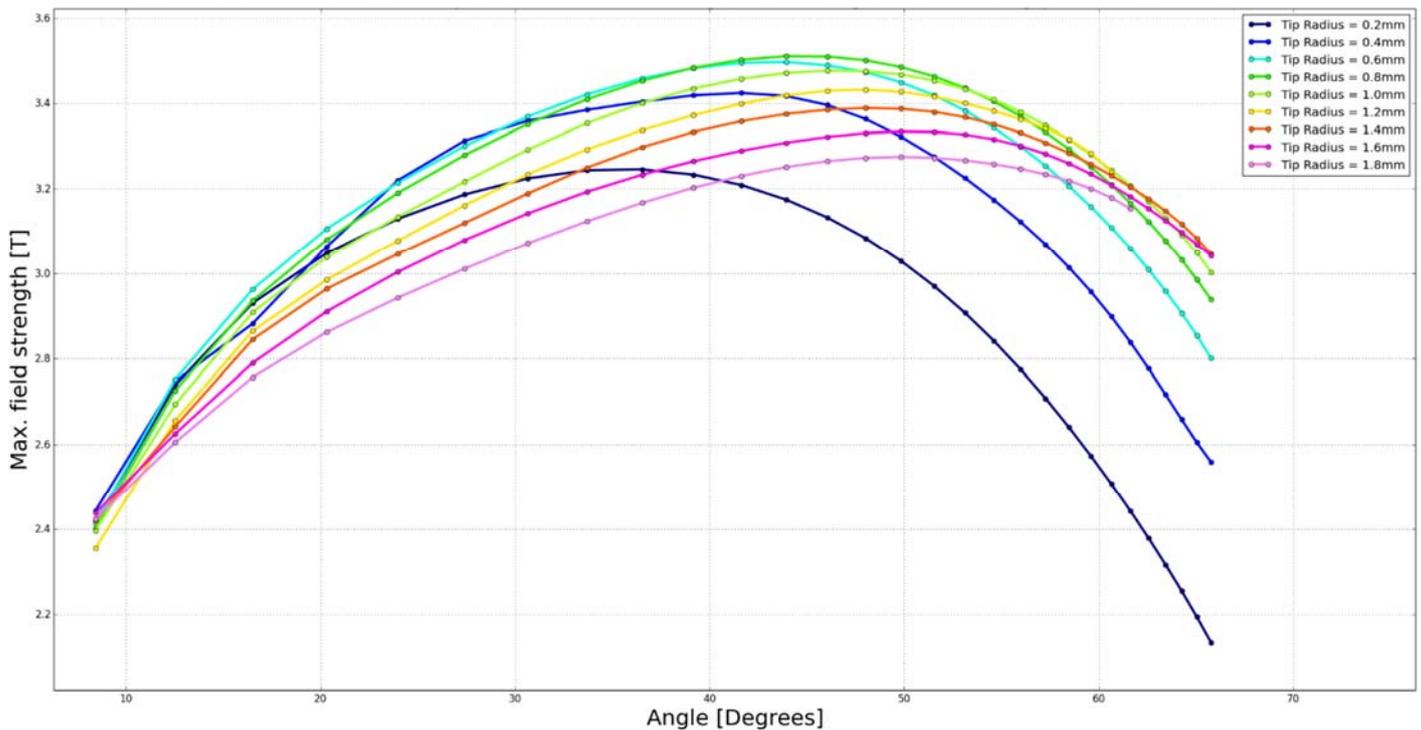
The effect of the different cone tip sizes is smaller than the one of the cone angles, but still we need to take it into account in order to generate a field higher than $3.0 \; T$.

If we define a ratio factor q (we re-introduced q which does not describe a charge now), which is defined as backside cone radius over the cone tip radius:

$$\frac{R_{Cone}}{R_{Tip}} = q \qquad (7.1)$$

We can read from the graph, that the perfect value for q is 25. Check the following table to see the changes in the field strength with an increasing or decreasing value for q. The value for the 1.6 mm tip size does not play along well, probably due to some numerical fluctuations. Not only the explanation given in the chapter "Single plots for the different cases", might be the answer. One should keep in mind, that these values are relatively close to each other and the q value is just introduced as an estimated factor. Also, the fact that a bigger cone tip makes the angle smaller by a little bit was neglected.

Cone tip radius [mm]	Maximum field [T]	Angle at max. field [°]	q value
0.2	3.24	26.8	100.0
0.4	3.34	40.9	50.0
0.6	3.50	33.8	33.3
0.8	3.52	36.1	25.0
1.0	3.48	34.4	20.0
1.2	3.44	38.6	16.7
1.4	3.40	37.0	14.3
1.6	3.43	33.1	12.5
1.8	3.27	44.7	11.1

The graph below shows maximum field strengths for their q values:
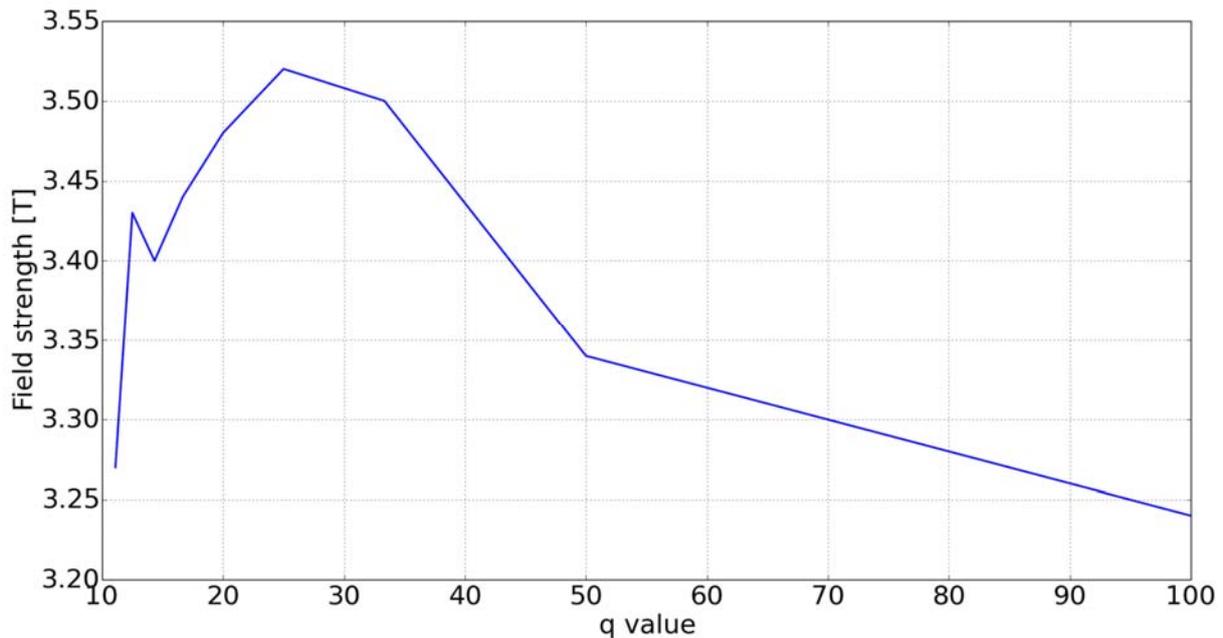
GRAPH 19: RELATION BETWEEN THE q VALUE AND THE CORRESPONDING FIELDS

The corresponding fields are measured with a hall sensor of HHP-MU, which is described in the chapter "Sensor". The setup itself was built within the laboratories of Vienna University of Technology. The pipe was milled from a high quality iron, the magnet is a standard high quality $Nd_2Fe_{14}B$ magnet, obtained from supermagnete.de (39). Both were described in the chapter "Materials".
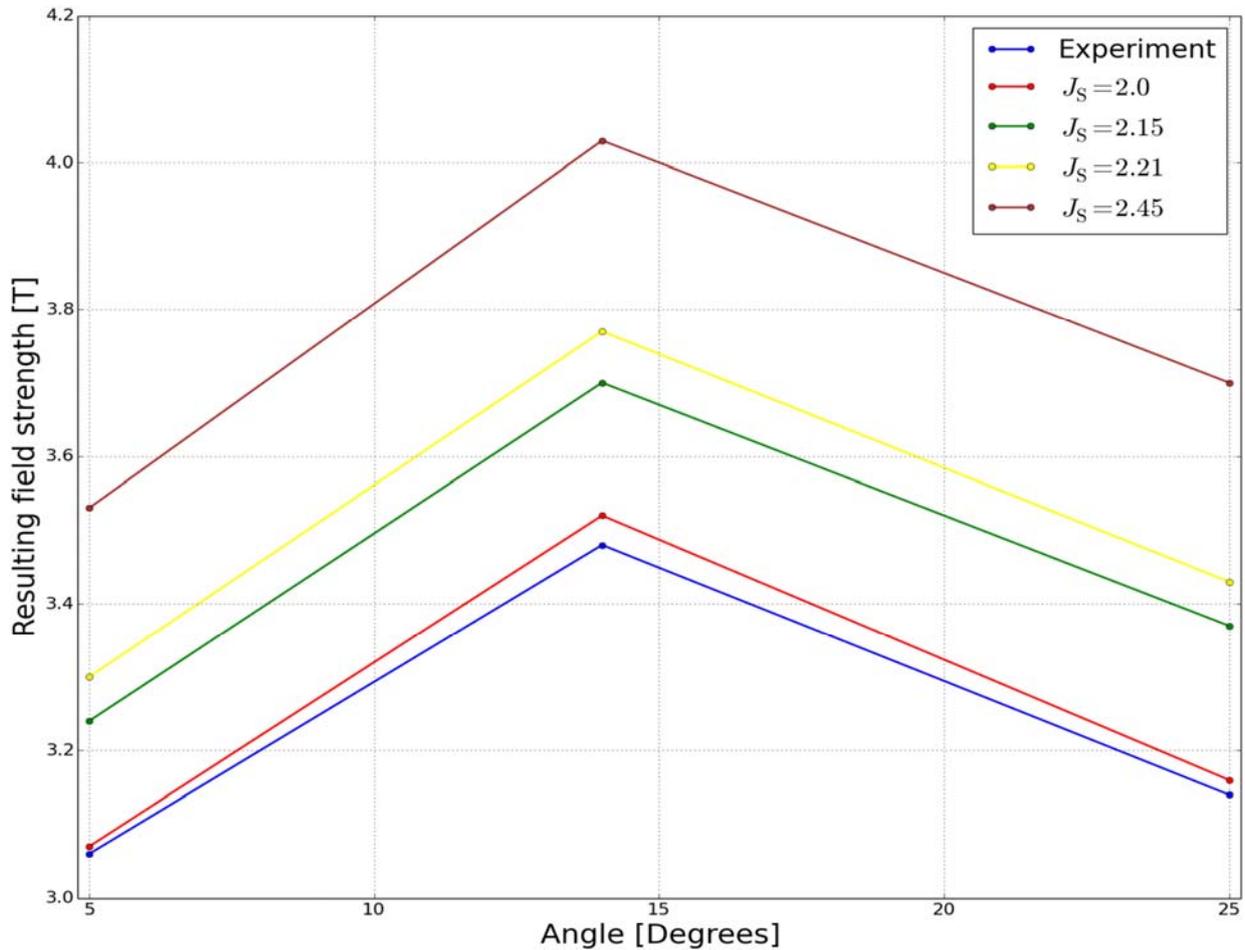
8. EXPERIMENTAL RESULTS

When coming from a simulation, the boundary conditions of an experiment place some limits (certainty of geometrical dimensions for example). It was intended to test with three different cones, but the Vienna University of Technology's workshop did have a hard time with milling and turning them into the defined shapes, which means the experimental data will be under the expected values. Fortunately, due to the nature of the simulation we can imply, that every error will just make our results worse – so the experimental case is somewhat of a lower limit for the field strengths to be expected, when working with the simulated setups.

Because of some deferments with the shipping of the iron and the second hysteresis measurement, the first simulations had to be done with an assumed value of $J_s = 2.0\ T$ which describes iron of average pureness.
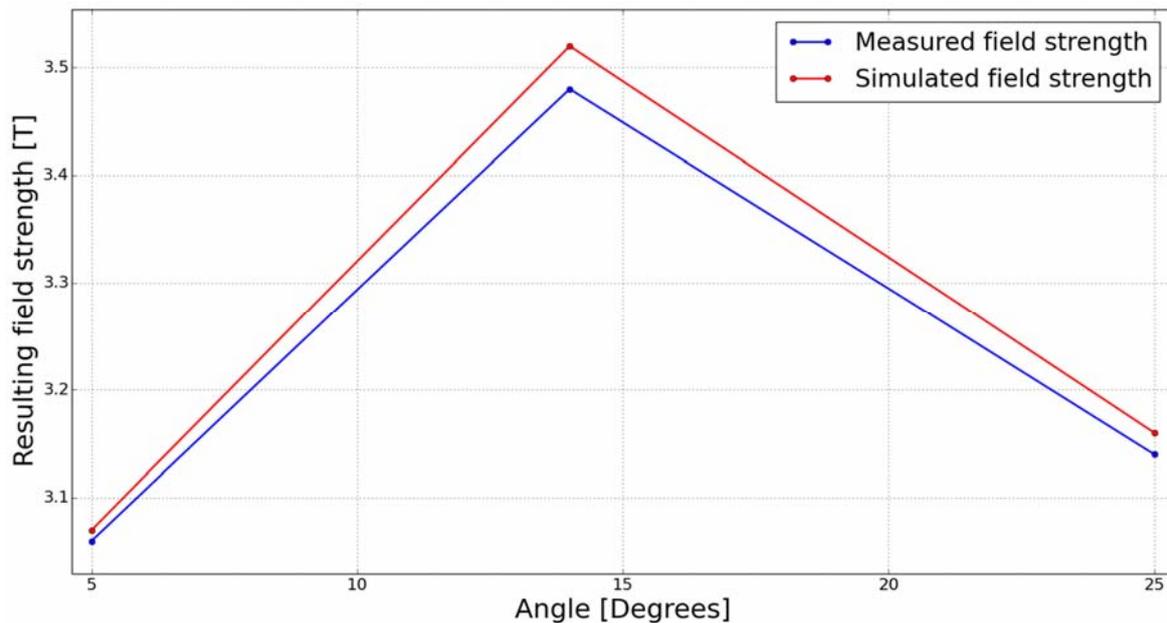
GRAPH 20: RESULTING FIELD STRENGTH OVER ANGLE FOR THE EXPERIMENT AND THE SIMULATION IN COMPARISON

After the experiment was finished, the three points of interest in Graph 20: Resulting field strength over angle for the experiment and the simulation in comparison were recomputed with the real value (as measured, see chapter "Iron-cones") $J_s = 2.15\ T$ and some other hypothetical values, to get an idea of how much one could expect a perfect experimental setup to perform.

GRAPH 21: SIMULATION RESULTS FOR HIGHER VALUES OF J_s

As Graph 21: Simulation results for higher values of J_s shows, the simulated field strengths are larger than the experimentally measured ones, although the difference is quite small usually, when using the values of $J_s = 2.0\ T$ (red line). At this point it is important to note, that $J_s = 2.15\ T$ (green line) values come from an interpolated method as described in the chapter "Iron-cones". This becomes even more interesting, when looking at the yellow line, for $J_s = 2.21\ T$ (the best value for pure iron, (49)) or even for materials with $J_s = 2.45\ T$ (brown line), which are used in modern hard drives for read heads ($CoFe$) alloys (50). Again, the values obtained from the experiment are shown by a blue line.

All experiments and simulations shown in this thesis are operated at room temperature. When not dependent on room temperature, one could use other rare earth metals like Gadolinium or Holmium, which have saturation magnetizations of $J \geq 4.0\ T$ (51) at very low temperatures.

TABLE 7: COMPARISON OF SIMULATED AND EXPERIMENTAL ACHIEVED FIELD STRENGTHS FOR DIFFERENT VALUES OF J_s

Cone Angle [°]	Simulated field strength [T]				Measured field strength [T]	Difference [%]	
	$J_s = 2.0$	$J_s = 2.15$	$J_s = 2.21$	$J_s = 2.45$		$J_s = 2.0$	$J_s = 2.15$
20.3	3.07	3.24	3.30	3.53	3.06	1.003	1.068
46.0	3.52	3.70	3.77	4.03	3.48	1.011	1.071
61.6	3.16	3.37	3.43	3.70	3.14	1.006	1.073

These measured values are very close to the simulated ones although in the experimental setup several of errors exists, such as:

- The cones are not perfectly flat on both ends
- The magnets were not facing each other perfectly
- Magnets and iron should be sanded to a very smooth surface
- The measured hysteresis loop is not an input parameter for the simulation – only two approximated points

9. CONCLUSION AND OUTLOOK

The computed values for the magnetization of the simulated arrangements were almost (less than 5%) achieved in the experiment – although it was done under no ideal conditions. The achieved maximum field measured was $3.48\,T$, which is far above the saturation of the used iron ($J_s = 2.15$ T, see chapter "Iron-cones"). As Graph 20: Resulting field strength over angle for the experiment and the simulation in comparison shows, the simulated and the experimentally achieved values are quite close to each other.

The most important question remaining is, if the other values with smaller air gaps in Graph 9: Comparison of the maximum fields at a perfect cone angle for increasing air gaps could also be confirmed by experiments. The next step would be an experiment capable ofo exceed $4.0\,T$, which is larger than two times J_s. In order to do so, a separate project would be necessary. For this experiment it is suggested to build an adjustable restraining device that is far more complex than the one used in this work. It should be able to move the magnets to the utter closest distance for the sensor to fit in the gap and remove them again with some comfort – so many different measurements can be made in a small amount of time. Also the sensor should be in a fixed position. Such an experiment is not feasible with the in house workshop of the Vienna University of Technology, so a company that can mill and turn more exact geometries is needed.

10. REFERENCES

1. **wikipedia.** physical constants. *wikipedia.* [Online] February 14, 2014. [Cited: April 10, 2014.] http://en.wikipedia.org/wiki/Physical_constant.

2. **Mayergoyz, Georgio Bertotti and Isaak D.** *The Science of Hysteresis, Vol. 1.* Oxford : Academic Press, 2006.

3. **Parker, Rollin J.** *Permanent Magnet Guidlines.* s.l. : Magnetic Materials Producers Association, 1998.

4. **Wolf, William P.** Cooling by adiabatic magnetization. *Physical Review 115.* 1959, pp. 1196-1197.

5. **Kanai, Yasushi et al.** Recording field analysis of narrow-track SPT head with side shields, tapered main pole, and tapered return path for 1 Tb/in 2. *Magnetics, IEEE Transactions 39.4.* 2003, pp. 1955-1960.

6. **Daughton, Jim et al.** Magnetic Field Sensors Using GMR Multilayer. *IEEE Transactions on Magnetics Vol 30 No. 6.* November 1994, pp. 4608-4610.

7. **Konrad Kapser, Markus Weinberger, Wolfgang Granig, Peter Slama.** *GMR Sensors in Automotive Applications, Vol. 6.* s.l. : Springer Berlin Heidelberg, 2013.

8. **Gaster, Richard S. et al.** Quantification of protein interactions and solution transport using high-density GMR sensor arrays. *Nature Nanotechnology, Vol. 6.* May 5, 2001, pp. 314-320.

9. **Daughton, Jim et al.** GMR Applications. *Journal of Magnetism and Magnetic Materials.* February 15, 1999, pp. 334-342.

10. **Lenz, James et al.** Magnetic Sensors and Their Applications. *IEEE Sensors Journal, Vol. 6, No. 3.* June 2006, pp. 631-649.

11. **SuessCo.** suessco.com. [Online] 2012. [Cited: April 10, 2014.] http://suessco.com/simulations/solutions/femme-software/.

12. **Aharoni, Amikan.** Demagnetizing factors for rectangular ferromagnetic prisms. *Journal of Applied Physics 83.6.* 1998, pp. 3432-3434.

13. **Osborne, James A.** Demagnetizing Factors of the General Ellipsoid. *Journal of Magnetism and Magnetic Materials 331.* 2013, pp. 187-192.

14. **Bogart, John W.C. Van.** *Magnetic Tape Storage and Handling.* Washington DC : The Commission on Preservation and Access and The National Media Laboratory, 1995. p. Appendix 5: Glossary.

15. **wikipedia.** wikipedia. [Online] April 11, 2014. [Cited: April 15, 2014.] http://en.wikipedia.org/wiki/Paleomagnetism.

16. **Chikazumi, Soshin.** *Physics of Ferromagnetism, 2nd edition.* s.l. : Oxford University Press, 1997.

17. **Leroy, Paul, et al.** High magnetic field amplification for improving the sensitivity of hall sensors. *Sensors Journal, IEEE 6.3.* 2006, pp. 707-713.

18. **Sen-ben Liao, Peter Dourmashkin, and John Belcher.** Physics 8.02 Electricity and Magnetism. *Course Notes and Vizualizations.* [Online] 2004. [Cited: May 1, 2014.] http://web.mit.edu/viz/EM/visualizations/coursenotes/.

19. **Jackson, John D.** *Classical Electrodynamics, 3rd edition.* s.l. : Walter de Gruyter, 1998.

20. **wikipedia.** Conversion between SI and CGS units. [Online] March 14, 2014. [Cited: April 10, 2014.] http://en.wikipedia.org/wiki/Magnetic_susceptibility#Conversion_between_SI_and_CGS_units.

21. **Myriam Pannetier, Claude Fermon, Gerald Le Goff, Juha Simola, Emma Kerr.** Femtotesla Magnetic Field Measurement with Magnetoresistive Sensors. *Science.* June 11, 2004, 304, pp. 1648-1650.

22. **Sensors, Advances in Magnetic Field.** Pavel Ripka and Michal Janosek. *IEEE SENSORS JOURNAL, VOL. 10, NO. 6, JUNE 2010.* June 2010, Vol. 6, 10, pp. 1108-1116.

23. **Pannetier-Lecoeur, M., et al.** RF Response of Superconducting-GMR Mixed Sensors, Application to NQR. *IEEE Transactions on Applied Superconductivity.* June 2007, Vol. 2, 17, pp. 598-601.

24. **Maxwell, James C.** Electricity and Magnetism, Vol. 2. Oxford : The Clarendon Press, 1904, pp. 66-70.

25. **wikipedia.** saturation (magnetic). [Online] January 29, 2014. [Cited: April 10, 2014.] http://en.wikipedia.org/wiki/Saturation_(magnetic).

26. **Bruckner, Florian.** *Multiscale Simulation of Magnetic Nanostructurs.* 2013.

27. **Bruckner Florian, Feischl Michael, Führer Thomas, Page Markus, Praetorius Dirk and Suess Dieter.** Combining micromagnetism and magnetostatic Maxwell equations for multiscale magnetic simulations. *Journal of Magnetism and Magnetic Materials, Volume 343.* October 2013, pp. 163-168.

28. **wikipedia.** wikipedia. [Online] April 3, 2014. [Cited: April 15, 2014.] http://en.wikipedia.org/wiki/Neodymium_magnet.

29. **Anders Logg, Kent-Andre Mardal, Garth Wells.** *Automated Solution of Differential Equations by the Finite Element Method - The FEniCS Book.* s.l. : Springer, 2012.

30. **Johnson, Claes.** *Numerical solution of partial differential equations by the finite element method.* Dover : Dover Pubn Inc, 2009.

31. **Bruckner Florian, Feischl Michael, Führer Thomas, Goldenits Petra, Page Marcus, Praetorius Dirk, Ruggeri Michele and Suess Dieter.** Multiscale modeling in micromagnetics: well-posedness and numerical integration. *arXiv:1209.5548.* 2012.

32. **Bruckner Florian, Vogler Christoph, Feischl Michael, Praetorius Dirk, Bergmair Bernhard, Huber Thomas, Fuger Markus and Suess Dieter.** 3D FEM-BEM-coupling method to solve magnetostatic Maxwell equations. *Journal of Magnetism and Magnetic Materials, Volume 324, Issue 10, .* May 2012, pp. 1862–1866.

33. **J. Fetzer, S. Abele and G. Lehner.** Die Kopplung der Randelementmethode und der Methode der finiten Elemente zur Lösung dreidimensionaler elektromagnetischer Feldprobleme auf unendlichem Grundgebiet . *Archiv für Elektrotechnik, Vol. 76.* 1993.

34. **wikipedia.** Dirichlet boundary condition. [Online] December 6, 2013. [Cited: April 17, 2014.] http://en.wikipedia.org/wiki/Dirichlet_boundary_condition.

35. **OPEN CASCADE SAS (EURIWARE group.** Salome. [Online] OPEN CASCADE SAS (EURIWARE group). [Cited: April 14, 2014.] http://www.salome-platform.org/.

36. **Schöberl, Joachim.** NETGEN. [Online] January 29, 2009. [Cited: April 10, 2014.] http://www.hpfem.jku.at/netgen/.

37. **Marinho, Zita.** *3D Magnetic Flux Concentrators with improved efficiency for Magnetoresistive Sensors.* Lisboa : s.n., 2010.

38. **Groessinger, Roland.** A critical examination of the law of approach to saturation. I. Fit procedure. *Physica Satatus Solidi (a), Vol. 66, No. 2.* 1994, pp. 665-674.

39. **supermagnete.de.** supermagnete.de. [Online] 2003. http://www.supermagnete.de/data_sheet_Q-25-25-13-N.pdf.

40. **Scholz, Werner.** Calculator for magnetostatic energy and demagnetizing factor. [Online] 2002. [Cited: April 10, 2014.] http://www.magpar.net/static/magpar/doc/html/demagcalc.html.

41. **AK Steel International.** Platform Creative Technology Midden Gelderland. [Online] 1927. [Cited: April 10, 2014.] http://www.pctmg.nl/uploads/API-Brochure.pdf.

42. **GoodFellow.** GoodFellow Online Katalog. [Online] 2010. [Cited: April 10, 2014.] http://www.goodfellow.com/catalogue/GFCatalogue.php?Language=G.

43. **Cain, M. Stewart and M. G.** *Ferroelectric Hysteresis Measurment & Analysis.* Manchester : National Physical Laboratory, 1999. NPL Report CMMT(A) 152.

44. **Oser, Peter.** *Ein Hysteresograph zur Charakterisierung weichmagnetischer Materialien.* Wien : s.n., 2008.

45. **Hui Zhang, Dechang Zeng and Zhongwu Liu.** The law of approach to saturation in ferromagnets originating from the magnetocrystalline anisotropy. *Journal of Magnetism and Magnetic Materials.* 2010, Vol. 322, 16, pp. 2375-2380.

46. **Lenz, James, and Edelstein, Alan S.** Magnetic sensors and their applications. *Sensors Journal, IEEE 6.3.* 2006, pp. 631-649.

47. **Hall, Edwin.** On a New Action of a Magnet on Electric Currents. *American Journal of Mathematics, Bd 2.* 1879, pp. 287–292.

48. **AREPOC.** Catalogue of Hall probes. [Online] 2011. [Cited: April 10, 2014.] http://www.arepoc.sk/uploaded/download/HallProbes.PDF.

49. **H. Danan, A. Herr and A. J. P. Meyer.** New Determination of the Saturation Magnetization of Nickel and Iron. *Journal of Applied Physics, Volume 39.2.* 1968, pp. 669-670.

50. **Sun, N. X., and S. X. Wang.** Soft high saturation magnetization (Fe 0.7 Co 0.3) 1-x N x thin films for inductive write heads. *Magnetics, IEEE Transactions on 36.5.* 2000, pp. 2506-2508.

51. **R. W. Hoard, S.C. Mance, R. L. Leber, E. N. Dader, M. R. Chaplin, K. Blair.** Field Enhancement of a 12.5-T Magnet using Holmium Poles. *IEEE Transactions on Magnetics.* 2, 1985, Vol. 21.

52. **wikipedia.** FEM. [Online] March 9, 2014. [Cited: April 10, 2014.] http://en.wikipedia.org/wiki/Finite_element_method.

ACKNOWLEDGMENT

When trying to finish a lot of work in a very short time, one depends on the good will of his coworkers. In Dieter Suess' office many people welcomed me and gave me all the support (and criticism) I needed to finish this work.

So before giving thanks to the people in charge, I want to thank Christoph, Claas, Florian and Roman, to always lend a helping hand, to always spare a minute (or many more) to tell me to do things correctly. Without your sarcasm and all the great fun we had, I would have left the Doppler Labor for Advanced Magnetic Sensing and Materials without a heavy heart.

There is no acknowledgment in a thesis without giving thanks to the professors: Many thanks to Roland Groessinger, who grew never tired of spending another hour discussing obvious stuff. And many more thanks to Dieter Suess, who did not know why and how exactly I ended up in his work group, but nevertheless motivated me even from the top of Mount Ararat and became a close friend in the last months.